

Sublattice-sensitive Majorana Modes

Di Zhu,^{1,*} Bo-Xuan Li,^{2,3,*} and Zhongbo Yan^{1,†}

¹*School of Physics, Sun Yat-Sen University, Guangzhou 510275, China*

²*Beijing National Laboratory for Condensed Matter Physics and Institute of Physics, Chinese Academy of Sciences, Beijing 100190, China*

³*University of Chinese Academy of Sciences, Beijing 100049, China*

(Dated: December 3, 2021)

For two- and three-dimensional topological insulators whose unit cells consist of multiple sublattices, the boundary terminating at which type of sublattice can affect the time-reversal invariant momentum at which the Dirac points of helical boundary states are located. Through a general theory and a representative model, we reveal that this interesting property allows the realization of Majorana modes at sublattice domain walls forming on the boundary when the boundary Dirac points of the topological insulator are gapped by an unconventional superconductor in proximity. Intriguingly, we find that the sensitive sublattice-dependence of the Majorana modes allows their positions to be precisely manipulated by locally controlling the terminating sublattices or boundary potential. Our work reveals that the common sublattice degrees of freedom in materials open a new route to realize and manipulate Majorana modes.

As a class of topological excitations, Majorana modes in topological superconductors (TSCs) have attracted tremendous research enthusiasm since a connection to fault-tolerant quantum computation was built [1, 2]. On the road to the final application in quantum computation, it is widely believed that a milestone will be the implementation of braiding Majorana zero modes (MZMs) [3], a type of bound-state Majorana modes. Historically, as MZMs was initially revealed to appear in the vortex cores of two dimensional chiral p -wave superconductors in the topological regime [4], the initial scenario for braiding MZMs is based on the natural idea of moving and exchanging vortices [5]. Later, theorists showed that the braiding process can also be carried out in networks of one-dimensional TSC wires [6, 7]. Despite being viewed as two most promising routes, an experimental realization of either one of them remains elusive till date. On one side, although steady and remarkable progress has been witnessed in the pursuit of MZMs in platforms ranging from semiconductor nanowires [8–18] and magnetic atom chains [19–21] to superconducting topological insulators [22–24] and iron-based superconductors [25–27], a decisive confirmation of MZMs in experiments has not been achieved. On the other hand, both scenarios require some levels of controllability on the positions of MZMs, however, manipulating vortex-core or wire-end MZMs in a highly controllable way itself is also rather challenging in experiments.

In the past few years, the birth of the concept named higher-order TSCs provides new perspectives for both the implementation and manipulation of both MZMs and other propagating Majorana modes [28–82]. A unique characteristic of higher-order TSCs is that the concomitant Majorana modes have a codimension (d_c) larger than one and their locations in real space depend on the boundary geometry, which is fundamentally distinct to conventional TSCs (also dubbed first-order TSCs) protected by internal symmetries only [83], where the Majorana modes have $d_c = 1$ and their locations do not rely on the boundary geometry as they appear everywhere on the whole boundary. Because of the freedom on the boundary, the positions of Majorana modes in a higher-order TSC are

in principle allowed to move if the Majorana modes are not pinned by any crystalline symmetry [31, 34]. Indeed, previous works have shown that the positions of MZMs in two-dimensional second-order TSCs can be tuned by rotating the orientation of magnetic field [35, 66, 84] or changing the boundary potential via electrical gating [62, 65], accordingly opening new routes to manipulate and braid MZMs [85–87]. In this work, we reveal that the sublattice degrees of freedom commonly appearing in materials admit a new intriguing scheme for the realization and manipulation of Majorana modes with $d_c = 2$. Remarkably, this scheme can be applied to systems both with and without time-reversal symmetry (TRS), and allows the positions of Majorana modes to be precisely manipulated.

As putting first-order topological insulators in proximity to unconventional superconductors can provide a natural realization of second-order TSCs [36–38], throughout this work we focus on this class of platforms to illustrate our theory. Accordingly, the physics can be roughly described as follows. For a d -dimensional first-order topological insulator with $d > 1$, while the appearance of helical states does not depend on the terminating sublattice type on the boundary [88, 89], a fact, interesting but having attracted little attention, is that the terminating sublattice type can affect the time-reversal invariant momentum (TRIM) at which the Dirac points of helical boundary states are located. On the other hand, it is known that the boundary Dirac points of a topological insulator can be gapped by the Dirac mass induced by the superconductor in proximity [90, 91]. Notably, if the superconducting pairing is momentum-dependent, both the magnitude and sign of the superconductivity-induced Dirac mass depend on the location of the boundary Dirac point. This indicates that the terminating sublattice type can directly affect the formation as well as the locations of domain walls binding Majorana modes. Below we first formulate the general theory from a boundary perspective, and then consider a two-dimensional topological insulator with honeycomb lattice and proximity-induced extended s -wave superconductivity to demonstrate the physics.

General theory from a boundary perspective.— Within

the mean-field framework, a superconducting system can be described by a corresponding Bogoliubov de-Gennes (BdG) Hamiltonian of the form $H = \frac{1}{2} \sum_{\mathbf{k}} \Psi_{\mathbf{k}}^\dagger [\mathcal{H}_N(\mathbf{k}) + \mathcal{H}_{SC}(\mathbf{k})] \Psi_{\mathbf{k}}$, where $\Psi_{\mathbf{k}}$ denotes the Nambu basis, \mathcal{H}_N describes the normal state, and \mathcal{H}_{SC} describes the superconducting pairing. When \mathcal{H}_N describes a first-order topological insulator with $d > 1$, one knows that helical states will appear on the boundary and form $(d-1)$ -dimensional Dirac points at TRIMs of the boundary Brillouin zone [88, 89]. If the chemical potential is set to locate at the Dirac point, then the low-energy Hamiltonian near the Dirac point for a given boundary terminating at a given type of sublattice will take the standard form [92]

$$\mathcal{H}_{\Gamma_s}(\mathbf{q}) = \sum_{i=1}^{d-1} v_i q_i \gamma_i, \quad (1)$$

where Γ_s denotes the TRIM at which the boundary Dirac point is located, \mathbf{q} is the momentum measured from Γ_s , and the γ_i matrices satisfy the Clifford algebra, i.e., $\{\gamma_i, \gamma_j\} = 2\delta_{ij}$. The effect from the superconducting pairing to the helical states can be determined by projecting \mathcal{H}_{SC} onto the subspace spanned by the orthogonal wave functions of helical boundary states. In general, if one only considers the leading-order contribution, what the superconducting pairing induces is a constant Dirac mass term to gap out the Dirac point. Accordingly, the low-energy physics on the boundary is described by a massive Dirac Hamiltonian of the form

$$\tilde{\mathcal{H}}_{\Gamma_s}(\mathbf{q}) = \sum_{i=1}^{d-1} v_i q_i \gamma_i + m_{\Gamma_s} \gamma_d, \quad (2)$$

with $\{\gamma_d, \gamma_{i=1, \dots, d-1}\} = 0$. Mathematically, the Dirac mass term is given by

$$[m_{\Gamma_s} \gamma_d]_{\alpha\beta} = \int dx_d \psi_\alpha^\dagger(x_d) \mathcal{H}_{SC}(-i\partial_{x_d}, \Gamma_s) \psi_\beta(x_d), \quad (3)$$

where $\{\psi_\alpha(x_d)\}$ denote the wave functions for the helical states localized at the x_d -normal boundary[93]. Focusing on the same boundary, if the location of the boundary Dirac point changes from Γ_s to $\Gamma_{s'}$ due to a change of the terminating sublattice type, then the boundary Hamiltonian will accordingly change to

$$\tilde{\mathcal{H}}_{\Gamma_{s'}}(\mathbf{q}') = \sum_{i=1}^{d-1} v'_i q'_i \gamma_i + m_{\Gamma_{s'}} \gamma_d, \quad (4)$$

where \mathbf{q}' denotes the momentum measured from $\Gamma_{s'}$. While the value of Fermi velocity for the helical states on a given boundary may also change, the sign cannot change as each branch of the helical states must propagate in a fixed direction. However, the superconductivity-induced Dirac mass can change its magnitude as well as the sign if the pairing has a momentum dependence, e.g., extended s-wave pairing, d-wave pairing etc. Without loss of generality, let us now consider a nonuniform boundary consisting of two parts which respectively terminate at two distinct types of sublattices. For

the convenience of discussion, we dub the interface separating two distinct types of terminating sublattices as *sublattice domain wall*. Assuming that the sublattice domain walls only break the translation symmetry of the given boundary in the x_{d-1} direction, the boundary Hamiltonian becomes

$$\mathcal{H}(-i\partial_{x_{d-1}}, \mathbf{q}'_{\parallel}) = -iv_{d-1}(x_{d-1})\gamma_{d-1}\partial_{x_{d-1}} + m(x_{d-1})\gamma_d + \sum_{i=1}^{d-2} v_i q'_i \gamma_i, \quad (5)$$

where $\mathbf{q}'_{\parallel} = (q'_1, \dots, q'_{d-2})$ denotes the momentum parallel to the sublattice domain walls. Notably, if m_{Γ_s} and $m_{\Gamma_{s'}}$ have opposite signs, then the Dirac mass $m(x_{d-1})$ will change sign across the sublattice domain walls. In other words, the sublattice domain walls are domain walls of Dirac mass. As a result, Majorana modes with $d_c = 2$ will emerge at the sublattice domain walls according to the Jackiw-Rebbi theory [94], corresponding to the realization of an extrinsic time-reversal invariant second-order TSC. As TRS is conserved, the resulting Majorana modes will be Majorana Kramers pairs (two MZMs related by TRS) in two dimensions [36, 37] and propagating helical Majorana modes in three dimensions [43].

The above general theory can be straightforwardly generalized to systems without TRS. Without loss of generality, let us consider that the TRS is broken by an external magnetic field. As Dirac mass induced by superconductivity and Zeeman field will compete, if $|m_{\Gamma_s}| \neq |m_{\Gamma_{s'}}|$ and the absolute value of the Zeeman-field-induced Dirac mass falls between $|m_{\Gamma_s}|$ and $|m_{\Gamma_{s'}}|$, the Dirac mass of domain walls will become dominated by Zeeman field on one side and by superconductivity on the other side [93]. As a result, the Majorana Kramers pairs and helical Majorana modes will respectively change to single MZMs and chiral Majorana modes, with their locations still bound at the sublattice domain walls [93]. With the established general theory in mind, below we consider a concrete realization to demonstrate the discussed physics.

Kane-Mele model with spin-singlet pairing.— Since two-dimensional honeycomb lattices with just two types of sublattices allow a simple illustration of the essential physics, below we consider the representative Kane-Mele model to describe the topological insulator and further assume a proximity-induced spin-singlet pairing. The full Hamiltonian has the form

$$\begin{aligned} H = & t \sum_{\langle ij \rangle, \alpha} c_{i, \alpha}^\dagger c_{j, \alpha} + i\lambda_{\text{so}} \sum_{\langle\langle ij \rangle\rangle, \alpha, \beta} \nu_{ij} c_{i, \alpha}^\dagger (s^z)_{\alpha\beta} c_{j, \beta} \\ & - \mu \sum_{i, \alpha} c_{i, \alpha}^\dagger c_{i, \alpha} + [\Delta_0 \sum_i c_{i, \uparrow}^\dagger c_{i, \downarrow}^\dagger + \sum_{\langle ij \rangle} \Delta_{1;ij} c_{i, \uparrow}^\dagger c_{j, \downarrow}^\dagger \\ & + \sum_{\langle\langle ij \rangle\rangle} \Delta_{2;ij} c_{i, \uparrow}^\dagger c_{j, \downarrow}^\dagger + h.c.], \end{aligned} \quad (6)$$

where $\langle ij \rangle$ and $\langle\langle ij \rangle\rangle$ refer to nearest-neighbor and next-nearest-neighbor sites. The first line corresponds to the Kane-Mele model which realizes a two-dimensional first-order topological insulator as long as the spin-orbit coupling coefficient λ_{so} is nonzero [95, 96]. μ is the chemical potential,

Δ_0 , $\Delta_{1;ij}$ and $\Delta_{2;ij}$ represent the on-site, nearest-neighbor and next-nearest-neighbor pairings, respectively. To have momentum dependence in the pairing, at least one of $\Delta_{1;ij}$ and $\Delta_{2;ij}$ needs to be nonzero. It is worth noting that according to the general theory, there is no constraint on the pairing type (a demonstration of the physics via d-wave pairing is provided in the supplemental material [93]). Without loss of generality, below we assume $\Delta_{1;ij} = \Delta_1$ and $\Delta_{2;ij} = \Delta_2$ for simplicity, corresponding to an extended s-wave pairing which preserves all crystalline symmetry of the normal-state Hamiltonian.

By a Fourier transformation to the momentum space and choosing the basis to be $\Psi_k^\dagger = (\psi_k^\dagger, \psi_{-k}^\dagger)$ with $\psi_k^\dagger = (c_{A,k,\uparrow}^\dagger, c_{B,k,\uparrow}^\dagger, c_{A,k,\downarrow}^\dagger, c_{B,k,\downarrow}^\dagger)$, the BdG Hamiltonian reads

$$\begin{aligned} \mathcal{H}(\mathbf{k}) = & t \sum_i [\cos(\mathbf{k} \cdot \mathbf{a}_i) \tau_z s_0 \sigma_x + \sin(\mathbf{k} \cdot \mathbf{a}_i) \tau_z s_0 \sigma_y] \\ & + 2\lambda_{s_0} \sum_i \sin(\mathbf{k} \cdot \mathbf{b}_i) \tau_0 s_z \sigma_z - \mu \tau_z s_0 \sigma_0 \\ & - \Delta_1 \sum_i [\cos(\mathbf{k} \cdot \mathbf{a}_i) \tau_y s_y \sigma_x + \sin(\mathbf{k} \cdot \mathbf{a}_i) \tau_y s_y \sigma_y] \\ & - [\Delta_0 + 2\Delta_2 \sum_i \cos(\mathbf{k} \cdot \mathbf{b}_i)] \tau_y s_y \sigma_0, \end{aligned} \quad (7)$$

where the Pauli matrices τ_i , s_i and σ_i act on the particle-hole, spin (\uparrow, \downarrow) and sublattice (A, B) degrees of freedom, respectively. The sum runs over $i = 1, 2, 3$, with the nearest-neighbor vectors $\mathbf{a}_1 = a(0, 1)$, $\mathbf{a}_2 = \frac{a}{2}(\sqrt{3}, -1)$, $\mathbf{a}_3 = \frac{a}{2}(-\sqrt{3}, -1)$, and a being the lattice constant (below we set $a = 1$ for notational simplicity). The next-nearest-neighbor vectors $\mathbf{b}_1 = \mathbf{a}_2 - \mathbf{a}_3$, $\mathbf{b}_2 = \mathbf{a}_3 - \mathbf{a}_1$ and $\mathbf{b}_3 = \mathbf{a}_1 - \mathbf{a}_2$ [97]. The Hamiltonian has TRS (the time-reversal operator $\mathcal{T} = i\tau_0 s_y \sigma_0 \mathcal{K}$ with \mathcal{K} the complex conjugate operator), particle-hole symmetry ($\mathcal{P} = \tau_x s_0 \sigma_0 \mathcal{K}$), and inversion symmetry ($I = \tau_0 s_0 \sigma_x$). Because the coexistence of TRS and inversion symmetry enforces Kramers degeneracy to the bulk bands, the first-order topology of the BdG Hamiltonian will always be trivial for the concerned spin-singlet pairing [70, 75, 98]. In previous works, it has been shown that a topological insulator with square lattice in proximity to an extended s-wave superconductor can realize a second-order TSC with Majorana Kramers pairs localized at the corners of a square sample [36]. Notably, therein the topological criterion requires either the hopping or the pairing to have crystalline anisotropy, because otherwise domain walls of Dirac mass cannot form on the boundary due to symmetry constraint. However, as we will show below, even though both the hopping and pairing are considered to be isotropic in Eq.(7), here domain walls of Dirac mass can still form on the boundary due to the sublattice degrees of freedom.

For the honeycomb lattice, there are two kinds of simple boundaries whose outermost sublattices only contain one type, which are known as zigzag and beard boundaries (see Figs.1(a)(b)). Let us first investigate the influence of the change of terminating sublattice type on a given boundary to the helical edge states of the normal state. To be specific, we consider a cylindrical geometry with periodic boundary con-

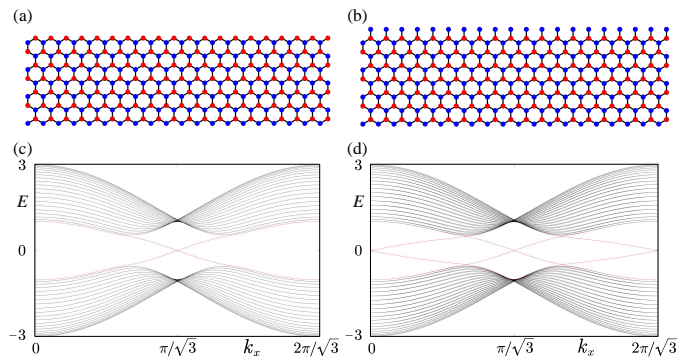


FIG. 1. (Color online) The sensitive dependence of boundary Dirac points on the terminating sublattice type. (a) The upper and lower zigzag edges of the lattice respectively terminate at sublattice B (red dots) and A (blue dots). (b) The lower edge keeps to be the same as in (a), but the upper edge changes to be a beard type, with the terminating sublattice type changing from B to A. (c) and (d) show the corresponding normal-state energy spectra when the y -normal open boundaries follow the structures shown in (a) and (b), respectively. In (c)(d), periodic boundary condition is assumed in the x direction, and parameters are $t = 1$, $\lambda_{s_0} = 0.1$.

dition in the x direction and open boundary condition in the y direction. When the upper edge terminates at type-B sublattices and the lower edge terminates at type-A sublattices (see Fig.1(a)), one finds that the boundary Dirac points for both upper and lower edges are located at $k_x = \pi/\sqrt{3}$, as shown in Fig.1(c). By only changing the terminating sublattice type on the upper edge, one finds that one boundary Dirac point is immediately shifted from $k_x = \pi/\sqrt{3}$ to $k_x = 0$, as shown in Figs.1(b)(d). Since nothing changes in the bulk as well as on the lower edge, the shifted Dirac point apparently corresponds to the upper edge, indicating the sensitive sublattice-dependence of boundary Dirac points.

Taking into account the superconductivity, numerical results show that the on-site pairing, nearest-neighbor pairing and next-nearest-neighbor pairing have rather different effects to the helical edge states, as shown in Fig.2. The on-site pairing, as expected, will induce a Dirac mass to gap out the Dirac points, irrespective of whether the edge is zigzag-type or beard-type, as shown in Fig.2(a). In sharp contrast, Fig.2(b) shows that the boundary Dirac points are intact to the nearest-neighbor pairing. Last, the next-nearest-neighbor pairing turns out to open a gap for the Dirac point of the zigzag boundary but not for that of the beard boundary, as shown in Fig.2(c). These results indicate when both Δ_0 and Δ_2 are finite, the gaps opened for the Dirac points at $k_x = 0$ and $k_x = \pi/\sqrt{3}$ can be different, as shown in Fig.2(d).

As the effect of the nearest-neighbor pairing to the helical edge states is negligible, below we set $\Delta_1 = 0$ for simplicity. To obtain the topological criterion for the emergence of domain walls binding Majorana modes, we follow the general theory and derive the low-energy boundary Hamiltonians for both zigzag and beard edges [93]. Focusing on the upper y -normal boundary and considering the case with $\mu = 0$

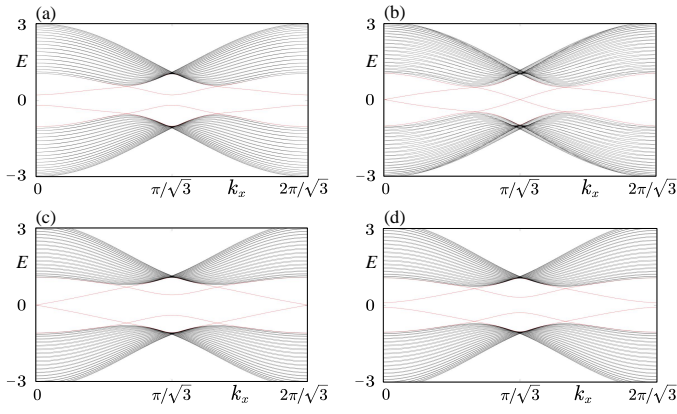


FIG. 2. (Color online) The energy spectrum of the BdG Hamiltonian for a cylindrical geometry with open (periodic) boundary condition in the $y(x)$ direction. The upper (lower) edge in the y direction is chosen to be the beard (zigzag) type. In (a)-(d), $t = 1$, $\lambda_{so} = 0.1$, $\mu = 0$, and pairing amplitudes are: (a) $\Delta_0 = 0.2$, $\Delta_1 = \Delta_2 = 0$; (b) $\Delta_1 = 0.2$, $\Delta_0 = \Delta_2 = 0$; (c) $\Delta_2 = 0.2$, $\Delta_0 = \Delta_1 = 0$; (d) $\Delta_0 = 0.1$, $\Delta_1 = 0$, $\Delta_2 = 0.2$.

for illustration, we find that the boundary Hamiltonian for the beard-type edge (terminating at type-A sublattices) is

$$\mathcal{H}_{u,\text{beard}}(q_x) = vq_x\tau_0s_z - \Delta_0\tau_ys_y, \quad (8)$$

where $v = 3\sqrt{3}\lambda_{so}$ and q_x is measured from $k_x = 0$, and the boundary Hamiltonian for the zigzag-type edge (terminating at type-B sublattices) is

$$\mathcal{H}_{u,\text{zigzag}}(q'_x) = v'q'_x\tau_0s_z + (2\Delta_2 - \Delta_0)\tau_ys_y, \quad (9)$$

where $v' \approx 6\sqrt{3}\lambda_{so}$ if $\lambda_{so}/t \ll 1$, and q'_x is measured from $k_x = \pi/\sqrt{3}$ [93]. It is easy to find that the Dirac masses in the two Hamiltonians will take opposite signs if $|\Delta_2| > |\Delta_0|/2 > 0$. This is the topological criterion for sublattice domain walls to host Majorana Kramers pairs at $\mu = 0$. Due to the robustness of topology, this topological criterion will hold as long as μ is lower than the critical value at which the boundary energy gap gets closed [93].

To validate the established topological criterion, we still consider a cylindrical geometry with periodic boundary condition in the x direction and just let the upper edge be nonuniform, with one part terminating at B-type sublattices (zigzag) and the other part terminating at A-type sublattices (beard). Accordingly, there are two sublattice domain walls on the upper edge, while the lower edge keeps uniform. As shown in Fig.3, when the topological criterion is fulfilled, a diagonalization of the Hamiltonian shows the existence of four MZMs, corresponding to two Majorana Kramers pairs. As expected, the wave functions of Majorana Kramers pairs are strongly localized around the sublattice domain walls. In addition, by a comparison of Figs.3(a) and (b), it is readily seen that the positions of Majorana Kramers pairs directly follow the change of the positions of sublattice domain walls, indicating that the positions of Majorana Kramers pairs can be tuned site-by-site

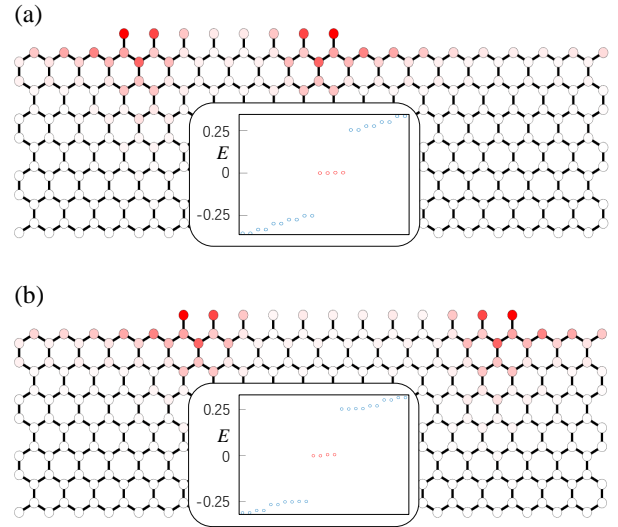


FIG. 3. (Color online) Majorana Kramers pairs bound at sublattice domain walls. Parameters in (a) and (b) are $t = 1$, $\lambda_{so} = 0.1$, $\mu = 0$, $\Delta_0 = \Delta_2 = 0.3$, $\Delta_1 = 0$. With periodic boundary condition in the x direction except for the uppermost beard-type part, the two insets in (a) and (b) show the corresponding energy spectra. The four dots highlighted by red indicate the existence of two Majorana Kramers pairs. The shade of the red color on the lattice sites reflect the weight of the probability density of Majorana Kramers pairs.

by a precise control of the terminating sublattices. Remarkably, even when the positions of sublattice domain walls are fixed, we find that the same goal can also be achieved by electrically tuning the local boundary potential [93].

Discussion and conclusion.— While our theory is exemplified in terms of the two-dimensional honeycomb lattice, its generality admits a wide application as sublattice degrees of freedom are rather common in materials, e.g., the class of materials with kagome or Lieb lattice consist of three types of sublattices [99, 100]. As a new scheme for the implementation of extrinsic second-order TSCs and Majorana modes, one remarkable merit is that the sensitive sublattice-dependence allows the positions of Majorana modes to be manipulated at an atomically precise level. Therefore, our work opens a promising avenue for achieving the manipulation and braiding of Majorana modes.

Acknowledgements.— We thank Zhi Wang for helpful discussions. This work is supported by the National Natural Science Foundation of China (Grant No.11904417 and 12174455) and the Natural Science Foundation of Guangdong Province (Grant No. 2021B1515020026).

* These authors contributed equally to this work.

† yanzhb5@mail.sysu.edu.cn

- [1] A.Yu. Kitaev, “Fault-tolerant quantum computation by anyons,” *Annals of Physics* **303**, 2–30 (2003).
 [2] Chetan Nayak, Steven H. Simon, Ady Stern, Michael Freed-

- man, and Sankar Das Sarma, “Non-abelian anyons and topological quantum computation,” *Rev. Mod. Phys.* **80**, 1083–1159 (2008).
- [3] Sankar Das Sarma, Michael Freedman, and Chetan Nayak, “Majorana zero modes and topological quantum computation,” *npj Quantum Information* **1**, 15001 (2015).
- [4] N. Read and Dmitry Green, “Paired states of fermions in two dimensions with breaking of parity and time-reversal symmetries and the fractional quantum hall effect,” *Phys. Rev. B* **61**, 10267–10297 (2000).
- [5] D. A. Ivanov, “Non-abelian statistics of half-quantum vortices in p -wave superconductors,” *Phys. Rev. Lett.* **86**, 268–271 (2001).
- [6] Jason Alicea, Yuval Oreg, Gil Refael, Felix von Oppen, and Matthew P. A. Fisher, “Non-abelian statistics and topological quantum information processing in 1d wire networks,” *Nature Physics* **7**, 412–417 (2011).
- [7] David Aasen, Michael Hell, Ryan V. Mishmash, Andrew Higginbotham, Jeroen Danon, Martin Leijnse, Thomas S. Jespersen, Joshua A. Folk, Charles M. Marcus, Karsten Flensberg, and Jason Alicea, “Milestones toward majorana-based quantum computing,” *Phys. Rev. X* **6**, 031016 (2016).
- [8] V. Mourik, K. Zuo, S. M. Frolov, S. R. Plissard, E. P. A. M. Bakkers, and L. P. Kouwenhoven, “Signatures of majorana fermions in hybrid superconductor-semiconductor nanowire devices,” *Science* **336**, 1003–1007 (2012).
- [9] Anindya Das, Yuval Ronen, Yonatan Most, Yuval Oreg, Moty Heiblum, and Hadas Shtrikman, “Zero-bias peaks and splitting in an al-inas nanowire topological superconductor as a signature of majorana fermions,” *Nature Physics* **8**, 887–895 (2012).
- [10] M. T. Deng, C. L. Yu, G. Y. Huang, M. Larsson, P. Caroff, and H. Q. Xu, “Anomalous zero-bias conductance peak in a nb-insb nanowire–nb hybrid device,” *Nano Letters* **12**, 6414–6419 (2012).
- [11] A. D. K. Finck, D. J. Van Harlingen, P. K. Mohseni, K. Jung, and X. Li, “Anomalous modulation of a zero-bias peak in a hybrid nanowire-superconductor device,” *Phys. Rev. Lett.* **110**, 126406 (2013).
- [12] Leonid P. Rokhinson, Xinyu Liu, and Jacek K. Furdyna, “The fractional a.c. josephson effect in a semiconductor-superconductor nanowire as a signature of majorana particles,” *Nature Physics* **8**, 795–799 (2012).
- [13] M. T. Deng, S. Vaitiekėnas, E. B. Hansen, J. Danon, M. Leijnse, K. Flensberg, J. Nygård, P. Krogstrup, and C. M. Marcus, “Majorana bound state in a coupled quantum-dot hybrid-nanowire system,” *Science* **354**, 1557–1562 (2016).
- [14] S. M. Albrecht, A. P. Higginbotham, M. Madsen, F. Kuemmeth, T. S. Jespersen, J. Nygård, P. Krogstrup, and C. M. Marcus, “Exponential protection of zero modes in majorana islands,” *Nature* **531**, 206–209 (2016).
- [15] Jun Chen, Peng Yu, John Stenger, Moira Hococevar, Diana Car, Sébastien R. Plissard, Erik P. A. M. Bakkers, Tudor D. Stanescu, and Sergey M. Frolov, “Experimental phase diagram of zero-bias conductance peaks in superconductor/semiconductor nanowire devices,” *Science Advances* **3**, e1701476 (2017).
- [16] Hao Zhang, Önder Gül, Sonia Conesa-Boj, Michał P. Nowak, Michael Wimmer, Kun Zuo, Vincent Mourik, Folkert K. de Vries, Jasper van Veen, Michiel W. A. de Moor, Jouri D. S. Bommer, David J. van Woerkom, Diana Car, Sébastien R. Plissard, Erik P.A.M. Bakkers, Marina Quintero-Pérez, Maja C. Cassidy, Sebastian Koelling, Srijit Goswami, Kenji Watanabe, Takashi Taniguchi, and Leo P. Kouwenhoven, “Ballistic superconductivity in semiconductor nanowires,” *Nature Communications* **8**, 16025 (2017).
- [17] Antonio Fornieri, Alexander M. Whiticar, F. Setiawan, Elías Portolés, Asbjørn C. C. Drachmann, Anna Keselman, Sergei Gronin, Candice Thomas, Tian Wang, Ray Kallagher, Geoffrey C. Gardner, Erez Berg, Michael J. Manfra, Ady Stern, Charles M. Marcus, and Fabrizio Nichele, “Evidence of topological superconductivity in planar josephson junctions,” *Nature* **569**, 89–92 (2019).
- [18] Hechen Ren, Falko Pientka, Sean Hart, Andrew T. Pierce, Michael Kosowsky, Lukas Lunczer, Raimund Schlereth, Benedikt Scharf, Ewelina M. Hankiewicz, Laurens W. Molenkamp, Bertrand I. Halperin, and Amir Yacoby, “Topological superconductivity in a phase-controlled josephson junction,” *Nature* **569**, 93–98 (2019).
- [19] Stevan Nadj-Perge, Ilya K. Drozdov, Jian Li, Hua Chen, Sangjun Jeon, Jungpil Seo, Allan H. MacDonald, B. Andrei Bernevig, and Ali Yazdani, “Observation of majorana fermions in ferromagnetic atomic chains on a superconductor,” *Science* **346**, 602–607 (2014).
- [20] Sangjun Jeon, Yonglong Xie, Jian Li, Zhijun Wang, B. Andrei Bernevig, and Ali Yazdani, “Distinguishing a majorana zero mode using spin-resolved measurements,” *Science* **358**, 772–776 (2017).
- [21] Howon Kim, Alexandra Palacio-Morales, Thore Posske, Levente Rózsa, Krisztián Palotás, László Szunyogh, Michael Thorwart, and Roland Wiesendanger, “Toward tailoring majorana bound states in artificially constructed magnetic atom chains on elemental superconductors,” *Science Advances* **4**, eaar5251 (2018).
- [22] Jin-Peng Xu, Mei-Xiao Wang, Zhi Long Liu, Jian-Feng Ge, Xiaojun Yang, Canhua Liu, Zhu An Xu, Dandan Guan, Chun Lei Gao, Dong Qian, Ying Liu, Qiang-Hua Wang, Fu-Chun Zhang, Qi-Kun Xue, and Jin-Feng Jia, “Experimental detection of a majorana mode in the core of a magnetic vortex inside a topological insulator-superconductor $\text{bi}_2\text{te}_3/\text{nbse}_2$ heterostructure,” *Phys. Rev. Lett.* **114**, 017001 (2015).
- [23] Hao-Hua Sun, Kai-Wen Zhang, Lun-Hui Hu, Chuang Li, Guan-Yong Wang, Hai-Yang Ma, Zhu-An Xu, Chun-Lei Gao, Dan-Dan Guan, Yao-Yi Li, Canhua Liu, Dong Qian, Yi Zhou, Liang Fu, Shao-Chun Li, Fu-Chun Zhang, and Jin-Feng Jia, “Majorana zero mode detected with spin selective andreev reflection in the vortex of a topological superconductor,” *Phys. Rev. Lett.* **116**, 257003 (2016).
- [24] Berthold Jäck, Yonglong Xie, Jian Li, Sangjun Jeon, B. Andrei Bernevig, and Ali Yazdani, “Observation of a majorana zero mode in a topologically protected edge channel,” *Science* **364**, 1255–1259 (2019).
- [25] Peng Zhang, Koichiro Yaji, Takahiro Hashimoto, Yuichi Ota, Takeshi Kondo, Kozo Okazaki, Zhijun Wang, Jinsheng Wen, GD Gu, Hong Ding, *et al.*, “Observation of topological superconductivity on the surface of an iron-based superconductor,” *Science* **360**, 182–186 (2018).
- [26] Dongfei Wang, Lingyuan Kong, Peng Fan, Hui Chen, Shiyu Zhu, Wenya Liu, Lu Cao, Yujie Sun, Shixuan Du, John Schneeloch, *et al.*, “Evidence for majorana bound states in an iron-based superconductor,” *Science* **362**, 333–335 (2018).
- [27] Qin Liu, Chen Chen, Tong Zhang, Rui Peng, Ya-Jun Yan, Chen-Hao-Ping Wen, Xia Lou, Yu-Long Huang, Jin-Peng Tian, Xiao-Li Dong, Guang-Wei Wang, Wei-Cheng Bao, Qiang-Hua Wang, Zhi-Ping Yin, Zhong-Xian Zhao, and Dong-Lai Feng, “Robust and clean majorana zero mode in the vortex core of high-temperature superconductor $(\text{li}_{0.84}\text{fe}_{0.16})\text{OHFeSe}$,” *Phys. Rev. X* **8**, 041056 (2018).

- [28] Wladimir A. Benalcazar, B. Andrei Bernevig, and Taylor L. Hughes, “Quantized electric multipole insulators,” *Science* **357**, 61–66 (2017).
- [29] Frank Schindler, Ashley M. Cook, Maia G. Vergniory, Zhijun Wang, Stuart S. P. Parkin, B. Andrei Bernevig, and Titus Neupert, “Higher-order topological insulators,” *Science Advances* **4** (2018), 10.1126/sciadv.aat0346.
- [30] Zhida Song, Zhong Fang, and Chen Fang, “ $(d - 2)$ -dimensional edge states of rotation symmetry protected topological states,” *Phys. Rev. Lett.* **119**, 246402 (2017).
- [31] Josias Langbehn, Yang Peng, Luka Trifunovic, Felix von Oppen, and Piet W. Brouwer, “Reflection-symmetric second-order topological insulators and superconductors,” *Phys. Rev. Lett.* **119**, 246401 (2017).
- [32] Hassan Shapourian, Yuxuan Wang, and Shinsei Ryu, “Topological crystalline superconductivity and second-order topological superconductivity in nodal-loop materials,” *Phys. Rev. B* **97**, 094508 (2018).
- [33] Eslam Khalaf, “Higher-order topological insulators and superconductors protected by inversion symmetry,” *Phys. Rev. B* **97**, 205136 (2018).
- [34] Max Geier, Luka Trifunovic, Max Hoskam, and Piet W. Brouwer, “Second-order topological insulators and superconductors with an order-two crystalline symmetry,” *Phys. Rev. B* **97**, 205135 (2018).
- [35] Xiaoyu Zhu, “Tunable majorana corner states in a two-dimensional second-order topological superconductor induced by magnetic fields,” *Phys. Rev. B* **97**, 205134 (2018).
- [36] Zhongbo Yan, Fei Song, and Zhong Wang, “Majorana corner modes in a high-temperature platform,” *Phys. Rev. Lett.* **121**, 096803 (2018).
- [37] Qiyue Wang, Cheng-Cheng Liu, Yuan-Ming Lu, and Fan Zhang, “High-temperature majorana corner states,” *Phys. Rev. Lett.* **121**, 186801 (2018).
- [38] Tao Liu, James Jun He, and Franco Nori, “Majorana corner states in a two-dimensional magnetic topological insulator on a high-temperature superconductor,” *Phys. Rev. B* **98**, 245413 (2018).
- [39] Yuxuan Wang, Mao Lin, and Taylor L. Hughes, “Weak-pairing higher order topological superconductors,” *Phys. Rev. B* **98**, 165144 (2018).
- [40] Chen-Hsuan Hsu, Peter Stano, Jelena Klinovaja, and Daniel Loss, “Majorana kramers pairs in higher-order topological insulators,” *Phys. Rev. Lett.* **121**, 196801 (2018).
- [41] Zhigang Wu, Zhongbo Yan, and Wen Huang, “Higher-order topological superconductivity: Possible realization in fermi gases and Sr_2RuO_4 ,” *Phys. Rev. B* **99**, 020508 (2019).
- [42] Yanick Volpez, Daniel Loss, and Jelena Klinovaja, “Second-order topological superconductivity in π -junction rashba layers,” *Phys. Rev. Lett.* **122**, 126402 (2019).
- [43] Rui-Xing Zhang, William S. Cole, and S. Das Sarma, “Helical hinge majorana modes in iron-based superconductors,” *Phys. Rev. Lett.* **122**, 187001 (2019).
- [44] Mason J. Gray, Josef Freudenstein, Shu Yang F. Zhao, Ryan O’Connor, Samuel Jenkins, Narendra Kumar, Marcel Hoek, Abigail Kopec, Soonsang Huh, Takashi Taniguchi, Kenji Watanabe, Ruidan Zhong, Changyoung Kim, G. D. Gu, and K. S. Burch, “Evidence for helical hinge zero modes in an fe-based superconductor,” *Nano Letters* **19**, 4890–4896 (2019).
- [45] Xiaoyu Zhu, “Second-order topological superconductors with mixed pairing,” *Phys. Rev. Lett.* **122**, 236401 (2019).
- [46] Yang Peng and Yong Xu, “Proximity-induced majorana hinge modes in antiferromagnetic topological insulators,” *Phys. Rev. B* **99**, 195431 (2019).
- [47] Rui-Xing Zhang, William S. Cole, Xianxin Wu, and S. Das Sarma, “Higher-order topology and nodal topological superconductivity in fe(se,te) heterostructures,” *Phys. Rev. Lett.* **123**, 167001 (2019).
- [48] Zhongbo Yan, “Higher-order topological odd-parity superconductors,” *Phys. Rev. Lett.* **123**, 177001 (2019).
- [49] Zhongbo Yan, “Majorana corner and hinge modes in second-order topological insulator/superconductor heterostructures,” *Phys. Rev. B* **100**, 205406 (2019).
- [50] Sayed Ali Akbar Ghorashi, Xiang Hu, Taylor L. Hughes, and Enrico Rossi, “Second-order dirac superconductors and magnetic field induced majorana hinge modes,” *Phys. Rev. B* **100**, 020509 (2019).
- [51] Nick Bultinck, B. Andrei Bernevig, and Michael P. Zaletel, “Three-dimensional superconductors with hybrid higher-order topology,” *Phys. Rev. B* **99**, 125149 (2019).
- [52] Song-Bo Zhang and Björn Trauzettel, “Detection of second-order topological superconductors by josephson junctions,” *Phys. Rev. Research* **2**, 012018 (2020).
- [53] Junyeong Ahn and Bohm-Jung Yang, “Higher-order topological superconductivity of spin-polarized fermions,” *Phys. Rev. Research* **2**, 012060 (2020).
- [54] Yi-Ting Hsu, William S. Cole, Rui-Xing Zhang, and Jay D. Sau, “Inversion-protected higher-order topological superconductivity in monolayer wTe_2 ,” *Phys. Rev. Lett.* **125**, 097001 (2020).
- [55] Ya-Jie Wu, Junpeng Hou, Yun-Mei Li, Xi-Wang Luo, Xiaoyan Shi, and Chuanwei Zhang, “In-plane zeeman-field-induced majorana corner and hinge modes in an s -wave superconductor heterostructure,” *Phys. Rev. Lett.* **124**, 227001 (2020).
- [56] Xiao-Hong Pan, Kai-Jie Yang, Li Chen, Gang Xu, Chao-Xing Liu, and Xin Liu, “Lattice-symmetry-assisted second-order topological superconductors and majorana patterns,” *Phys. Rev. Lett.* **123**, 156801 (2019).
- [57] S. Franca, D. V. Efremov, and I. C. Fulga, “Phase-tunable second-order topological superconductor,” *Phys. Rev. B* **100**, 075415 (2019).
- [58] Majid Kheirkhah, Yuki Nagai, Chun Chen, and Frank Marsiglio, “Majorana corner flat bands in two-dimensional second-order topological superconductors,” *Phys. Rev. B* **101**, 104502 (2020).
- [59] Majid Kheirkhah, Zhongbo Yan, Yuki Nagai, and Frank Marsiglio, “First- and second-order topological superconductivity and temperature-driven topological phase transitions in the extended hubbard model with spin-orbit coupling,” *Phys. Rev. Lett.* **125**, 017001 (2020).
- [60] Bitan Roy, “Higher-order topological superconductors in \mathcal{P} -, \mathcal{T} -odd quadrupolar dirac materials,” *Phys. Rev. B* **101**, 220506 (2020).
- [61] Katharina Laubscher, Danial Chughtai, Daniel Loss, and Jelena Klinovaja, “Kramers pairs of majorana corner states in a topological insulator bilayer,” *Phys. Rev. B* **102**, 195401 (2020).
- [62] Song-Bo Zhang, Alessio Calzona, and Björn Trauzettel, “All-electrically tunable networks of majorana bound states,” *Phys. Rev. B* **102**, 100503 (2020).
- [63] DinhDuy Vu, Rui-Xing Zhang, and S. Das Sarma, “Time-reversal-invariant C_2 -symmetric higher-order topological superconductors,” *Phys. Rev. Research* **2**, 043223 (2020).
- [64] Xianxin Wu, Wladimir A. Benalcazar, Yinxiang Li, Ronny Thomale, Chao-Xing Liu, and Jiangping Hu, “Boundary-obstructed topological high- t_c superconductivity in iron pnictides,” *Phys. Rev. X* **10**, 041014 (2020).
- [65] Xianxin Wu, Xin Liu, Ronny Thomale, and Chao-Xing Liu,

- “High- T_c superconductor Fe(Se,Te) Monolayer: an intrinsic, scalable and electrically-tunable majorana platform,” National Science Review (2021), 10.1093/nsr/nwab087, nwab087.
- [66] Tudor E. Pahomi, Manfred Sigrist, and Alexey A. Soluyanov, “Braiding majorana corner modes in a second-order topological superconductor,” Phys. Rev. Research **2**, 032068 (2020).
- [67] Apoorv Tiwari, Ammar Jahin, and Yuxuan Wang, “Chiral dirac superconductors: Second-order and boundary-obstructed topology,” Phys. Rev. Research **2**, 043300 (2020).
- [68] S. Ikegaya, W. B. Rui, D. Manske, and Andreas P. Schnyder, “Tunable majorana corner modes in noncentrosymmetric superconductors: Tunneling spectroscopy and edge imperfections,” Phys. Rev. Research **3**, 023007 (2021).
- [69] Majid Kheirkhah, Zhongbo Yan, and Frank Marsiglio, “Vortex-line topology in iron-based superconductors with and without second-order topology,” Phys. Rev. B **103**, L140502 (2021).
- [70] Bo-Xuan Li and Zhongbo Yan, “Boundary topological superconductors,” Phys. Rev. B **103**, 064512 (2021).
- [71] Yu-Biao Wu, Guang-Can Guo, Zhen Zheng, and Xu-Bo Zou, “Multiorder topological superfluid phase transitions in a two-dimensional optical superlattice,” Phys. Rev. A **104**, 013306 (2021).
- [72] Yu-Xuan Li and Tao Zhou, “Rotational symmetry breaking and partial majorana corner states in a heterostructure based on high- T_c superconductors,” Phys. Rev. B **103**, 024517 (2021).
- [73] Bo Fu, Zi-Ang Hu, Chang-An Li, Jian Li, and Shun-Qing Shen, “Chiral majorana hinge modes in superconducting dirac materials,” Phys. Rev. B **103**, L180504 (2021).
- [74] Kirill Plekhanov, Niclas Müller, Yanick Volpez, Dante M. Kennes, Herbert Schoeller, Daniel Loss, and Jelena Klinovaja, “Quadrupole spin polarization as signature of second-order topological superconductors,” Phys. Rev. B **103**, L041401 (2021).
- [75] Majid Kheirkhah, Zheng-Yang Zhuang, Joseph Maciejko, and Zhongbo Yan, “Surface Majorana Cones and Helical Majorana Hinge Modes in Superconducting Dirac Semimetals,” arXiv e-prints , arXiv:2107.02811 (2021), arXiv:2107.02811 [cond-mat.supr-con].
- [76] Arnob Kumar Ghosh, Tanay Nag, and Arijit Saha, “Hierarchy of higher-order topological superconductors in three dimensions,” Phys. Rev. B **104**, 134508 (2021).
- [77] Xun-Jiang Luo, Xiao-Hong Pan, and Xin Liu, “Higher-order topological superconductors based on weak topological insulators,” Phys. Rev. B **104**, 104510 (2021).
- [78] Aaron Chew, Yijie Wang, B. Andrei Bernevig, and Zhi-Da Song, “Higher-Order Topological Superconductivity in Twisted Bilayer Graphene,” arXiv e-prints , arXiv:2108.05373 (2021), arXiv:2108.05373 [cond-mat.supr-con].
- [79] Yi Tan, Zhi-Hao Huang, and Xiong-Jun Liu, “Edge geometric phase mechanism for second-order topological insulator and superconductor,” arXiv e-prints , arXiv:2106.12507 (2021), arXiv:2106.12507 [cond-mat.supr-con].
- [80] Ammar Jahin, Apoorv Tiwari, and Yuxuan Wang, “Higher-order topological superconductors from Weyl semimetals,” arXiv e-prints , arXiv:2103.05010 (2021), arXiv:2103.05010 [cond-mat.supr-con].
- [81] Tommy Li, Max Geier, Julian Ingham, and Harley D. Scammell, “Higher-order topological superconductivity from repulsive interactions in kagome and honeycomb systems,” arXiv e-prints , arXiv:2108.10897 (2021), arXiv:2108.10897 [cond-mat.supr-con].
- [82] Harley D. Scammell, Julian Ingham, Max Geier, and Tommy Li, “Intrinsic first and higher-order topological superconductivity in a doped topological insulator,” arXiv e-prints , arXiv:2111.07252 (2021), arXiv:2111.07252 [cond-mat.supr-con].
- [83] Ching-Kai Chiu, Jeffrey C. Y. Teo, Andreas P. Schnyder, and Shinsei Ryu, “Classification of topological quantum matter with symmetries,” Rev. Mod. Phys. **88**, 035005 (2016).
- [84] Liu Yang, Alessandro Principi, and Niels R. Walet, “Rotating Majorana Zero Modes in a disk geometry,” arXiv e-prints , arXiv:2109.03549 (2021), arXiv:2109.03549 [quant-ph].
- [85] Song-Bo Zhang, W. B. Rui, Alessio Calzona, Sang-Jun Choi, Andreas P. Schnyder, and Björn Trauzettel, “Topological and holonomic quantum computation based on second-order topological superconductors,” Phys. Rev. Research **2**, 043025 (2020).
- [86] Matthew F. Lapa, Meng Cheng, and Yuxuan Wang, “Symmetry-protected gates of Majorana qubits in a high- T_c higher-order topological superconductor platform,” SciPost Phys. **11**, 86 (2021).
- [87] Xiao-Hong Pan, Xun-Jiang Luo, Jin-Hua Gao, and Xin Liu, “Braiding higher-order majorana corner states through their spin degree of freedom,” arXiv:2111.12359 (2021).
- [88] M. Z. Hasan and C. L. Kane, “*Colloquium* : Topological insulators,” Rev. Mod. Phys. **82**, 3045–3067 (2010).
- [89] Xiao-Liang Qi and Shou-Cheng Zhang, “Topological insulators and superconductors,” Rev. Mod. Phys. **83**, 1057–1110 (2011).
- [90] Liang Fu and C. L. Kane, “Superconducting proximity effect and majorana fermions at the surface of a topological insulator,” Phys. Rev. Lett. **100**, 096407 (2008).
- [91] Liang Fu and C. L. Kane, “Josephson current and noise at a superconductor/quantum-spin-hall-insulator/superconductor junction,” Phys. Rev. B **79**, 161408 (2009).
- [92] Shun-Qing Shen, *Topological Insulators: Dirac Equation in Condensed Matters*, Vol. 174 (Springer Science & Business Media, 2013).
- [93] The supplemental material contains the details of: (i) the derivation of low-energy boundary Hamiltonians; (ii) d-wave pairing case; (iii) the impact of chemical potential on the boundary topological criterion; (iv) sublattice-sensitive Majorana zero modes in time-reversal symmetry broken systems; (v) manipulating the positions of Majorana zero modes by controlling the local boundary potential.
- [94] R. Jackiw and C. Rebbi, “Solitons with fermion number $1/2$,” Phys. Rev. D **13**, 3398–3409 (1976).
- [95] C. L. Kane and E. J. Mele, “Quantum spin hall effect in graphene,” Phys. Rev. Lett. **95**, 226801 (2005).
- [96] C. L. Kane and E. J. Mele, “ Z_2 topological order and the quantum spin hall effect,” Phys. Rev. Lett. **95**, 146802 (2005).
- [97] F. D. M. Haldane, “Model for a quantum hall effect without landau levels: Condensed-matter realization of the “parity anomaly”,” Phys. Rev. Lett. **61**, 2015–2018 (1988).
- [98] Xiao-Liang Qi, Taylor L. Hughes, and Shou-Cheng Zhang, “Topological invariants for the fermi surface of a time-reversal-invariant superconductor,” Phys. Rev. B **81**, 134508 (2010).
- [99] H.-M. Guo and M. Franz, “Topological insulator on the kagome lattice,” Phys. Rev. B **80**, 113102 (2009).
- [100] C. Weeks and M. Franz, “Topological insulators on the lieb and perovskite lattices,” Phys. Rev. B **82**, 085310 (2010).

Supplemental Material “Sublattice-sensitive Majorana Modes”

Di Zhu^{1,*}, Bo-Xuan Li^{2,3,*}, Zhongbo Yan^{1,†}

¹*School of Physics, Sun Yat-Sen University, Guangzhou, 510275, China*

²*Beijing National Laboratory for Condensed Matter Physics and Institute of Physics, Chinese Academy of Sciences, Beijing 100190, China*

³*University of Chinese Academy of Sciences, Beijing 100049, China*

This supplemental material contains five sections, including: (I) the derivation of low-energy boundary Hamiltonians for beard and zigzag edges; (II) two-dimensional honeycomb-lattice topological insulators in proximity to d-wave superconductors; (III) the impact of finite chemical potential on the topological criterion; (IV) sublattice-sensitive Majorana modes in time-reversal symmetry broken systems; (V) manipulating the positions of Majorana zero modes by electrically controlling the local boundary potential.

I. THE DERIVATION OF LOW-ENERGY BOUNDARY HAMILTONIANS FOR BEARD AND ZIGZAG EDGES

To derive the low-energy boundary Hamiltonian, we write down the bulk Bogoliubov-de Gennes (BdG) Hamiltonian in an explicit form, which reads

$$\begin{aligned}
\mathcal{H}_{\text{BdG}}(\mathbf{k}) = & t(2 \cos \frac{\sqrt{3}k_x}{2} \cos \frac{k_y}{2} + \cos k_y)\tau_z s_0 \sigma_x - t(2 \cos \frac{\sqrt{3}k_x}{2} \sin \frac{k_y}{2} - \sin k_y)\tau_z s_0 \sigma_y \\
& + 2\lambda_{so}(\sin \sqrt{3}k_x - 2 \sin \frac{\sqrt{3}k_x}{2} \cos \frac{3k_y}{2})\tau_0 s_z \sigma_z - \mu\tau_z s_0 \sigma_0 \\
& - \Delta_1(2 \cos \frac{\sqrt{3}k_x}{2} \cos \frac{k_y}{2} + \cos k_y)\tau_y s_y \sigma_x + \Delta_1(2 \cos \frac{\sqrt{3}k_x}{2} \sin \frac{k_y}{2} - \sin k_y)\tau_y s_y \sigma_y \\
& - [\Delta_0 + 2\Delta_2(\cos \sqrt{3}k_x + 2 \cos \frac{\sqrt{3}k_x}{2} \cos \frac{3k_y}{2})]\tau_y s_y \sigma_0.
\end{aligned} \tag{S1}$$

For notational simplicity, we have set the lattice constant to unity. For the convenience of discussion, throughout this work, t and λ_{so} will be assumed to be positive. As we have shown numerically that the nearest-neighbor pairing has a negligible effect to the helical edge states, below we also set $\Delta_1 = 0$ for simplicity.

According to numerical results, we know that for a cylindrical geometry with periodic boundary condition in the x direction and open boundary condition in the y direction, the boundary Dirac point, which corresponds to the crossing point of the energy spectrum of the normal-state helical edge states, is located at $k_x = 0$ ($k_x = \pi/\sqrt{3}$) for a beard (zigzag) edge. Below let us focus on the upper y -normal boundary and derive the corresponding low-energy boundary Hamiltonians for both beard and zigzag edges.

A. Low-energy boundary Hamiltonian for the beard edge

When the upper boundary is a beard edge, the terminating sublattices are type A. As numerical calculations reveal that the boundary Dirac point for such an edge will appear at $k_x = 0$, in order to derive the low-energy boundary Hamiltonian, we perform an expansion of the bulk Hamiltonian around $k_x = 0$ up to the linear order in momentum. Accordingly, the Hamiltonian becomes

$$\begin{aligned}
\mathcal{H}_{\text{BdG}}(q_x, k_y) = & t(2 \cos \frac{k_y}{2} + \cos k_y)\tau_z s_0 \sigma_x - t(2 \sin \frac{k_y}{2} - \sin k_y)\tau_z s_0 \sigma_y \\
& + 2\sqrt{3}\lambda_{so}q_x(1 - \cos \frac{3k_y}{2})\tau_0 s_z \sigma_z - \mu\tau_z s_0 \sigma_0 \\
& - [\Delta_0 + 2\Delta_2(1 + 2 \cos \frac{3k_y}{2})]\tau_y s_y \sigma_0,
\end{aligned} \tag{S2}$$

where q_x denotes a small momentum measured from $k_x = 0$. Next, we decompose the Hamiltonian into two parts, $\mathcal{H}_{\text{BdG}} = \mathcal{H}_1 + \mathcal{H}_2$, with

$$\begin{aligned}
\mathcal{H}_1(q_x, k_y) = & t(2 \cos \frac{k_y}{2} + \cos k_y)\tau_z s_0 \sigma_x - t(2 \sin \frac{k_y}{2} - \sin k_y)\tau_z s_0 \sigma_y, \\
\mathcal{H}_2(q_x, k_y) = & 2\sqrt{3}\lambda_{so}q_x(1 - \cos \frac{3k_y}{2})\tau_0 s_z \sigma_z - \mu\tau_z s_0 \sigma_0 - [\Delta_0 + 2\Delta_2(1 + 2 \cos \frac{3k_y}{2})]\tau_y s_y \sigma_0.
\end{aligned} \tag{S3}$$

For real materials, $\lambda_{so} \ll t$ and $\Delta_{0,2} \ll t$ are naturally satisfied. As we are interested in the regime where q_x is small, the whole \mathcal{H}_2 can be treated as a perturbation if the chemical potential is also assumed to be close to the neutrality condition.

In the following, let us consider a half-infinity sample with the boundary corresponding to the upper beard edge. In the basis $\Psi_{q_x} = (c_{1,A,q_x}, c_{1,B,q_x}, c_{2,A,q_x}, c_{2,B,q_x}, \dots, c_{n,A,q_x}, c_{n,B,q_x}, \dots)^T$ with $c_{n,A(B),q_x} = (c_{n,A(B),q_x,\uparrow}, c_{n,A(B),q_x,\downarrow}, c_{n,A(B),-q_x,\uparrow}^\dagger, c_{n,A(B),-q_x,\downarrow}^\dagger)$, the Hamiltonian in the matrix form reads

$$\mathcal{H}_1 = \begin{pmatrix} 0 & t\tau_z s_0 & 0 & 0 & 0 & 0 & \cdots \\ t\tau_z s_0 & 0 & 2t\tau_z s_0 & 0 & 0 & 0 & \cdots \\ 0 & 2t\tau_z s_0 & 0 & t\tau_z s_0 & 0 & 0 & \cdots \\ 0 & 0 & t\tau_z s_0 & 0 & 2t\tau_z s_0 & 0 & \cdots \\ 0 & 0 & 0 & 2t\tau_z s_0 & 0 & t\tau_z s_0 & \cdots \\ 0 & 0 & 0 & 0 & t\tau_z s_0 & 0 & \cdots \\ \vdots & \vdots & \vdots & \vdots & \vdots & \vdots & \ddots \end{pmatrix}. \quad (\text{S4})$$

To see that this Hamiltonian has solutions for zero-energy bound states, we solve the eigenvalue equation $\mathcal{H}_1|\Psi_\alpha\rangle = 0$. Concretely, as τ_z and s_z both commute with \mathcal{H}_1 , the eigenvector $|\Psi_\alpha\rangle$ can be assigned with the form

$$|\Psi_{\tau s}\rangle = |\tau_z = \tau\rangle \otimes |s_z = s\rangle \otimes (\psi_{1A}, \psi_{1B}, \psi_{2A}, \psi_{2B}, \dots, \psi_{nA}, \psi_{nB}, \dots)^T, \quad (\text{S5})$$

where $\tau = \pm 1$ and $s = \pm 1$ correspond to the two possible eigenvalues of τ_z and s_z , respectively. Taking the expression of $|\Psi_{\tau s}\rangle$ back into the eigenvalue equation $\mathcal{H}_1|\Psi_{\tau s}\rangle = 0$, one gets a series of equations with periodic structures, which read

$$\begin{aligned} t_\tau \psi_{1B} &= 0, \\ t_\tau \psi_{1A} + 2t_\tau \psi_{2A} &= 0, \\ 2t_\tau \psi_{1B} + t_\tau \psi_{2B} &= 0, \\ &\dots \\ t_\tau \psi_{nA} + 2t_\tau \psi_{(n+1)A} &= 0, \\ 2t_\tau \psi_{nB} + t_\tau \psi_{(n+1)B} &= 0, \\ &\dots, \end{aligned} \quad (\text{S6})$$

where $t_\tau \equiv t\tau$. According to the periodic structures, one can easily find

$$\psi_{(n+1)A} = -\frac{1}{2}\psi_{nA}, \quad \psi_{nB} = 0. \quad (\text{S7})$$

Therefore, the eigenvectors take the form

$$|\Psi_{\tau s}\rangle = |\tau_z = \tau\rangle \otimes |s_z = s\rangle \otimes \mathcal{N}(1, 0, -\frac{1}{2}, 0, \dots, (-\frac{1}{2})^{(n-1)}, 0, \dots)^T, \quad (\text{S8})$$

where the normalization constant \mathcal{N} is determined by the normalization condition $\langle \Psi_{\tau s} | \Psi_{\tau s} \rangle = 1$. Simple algebra calculations give

$$\mathcal{N}^2 \sum_{n=0}^{\infty} \frac{1}{2^{2n}} = \mathcal{N}^2 \frac{1}{1 - \frac{1}{4}} = \frac{4}{3} \mathcal{N}^2 = 1, \quad (\text{S9})$$

indicating $\mathcal{N} = \frac{\sqrt{3}}{2}$. As ψ_{nA} decays in a power law with the increase of n , the existence of four such eigenvectors indicates the existence of four zero-energy bound states. It is worth noting that the topological insulator has one pair of helical states on a given edge, but the introduce of particle-hole degrees of freedom doubles the number of helical states. Next, we project \mathcal{H}_2 onto the basis spanned by the four zero-energy eigenvectors. To proceed, we write down the matrix form for each term in \mathcal{H}_2 .

Let us first focus on the term $\mathcal{H}_{2,1} = 2\sqrt{3}\lambda_{so}q_x(1 - \cos \frac{3k_y}{2})\tau_0 s_z \sigma_z$. In the basis $\Psi_{q_x} = (c_{1,A,q_x}, c_{1,B,q_x}, c_{2,A,q_x}, c_{2,B,q_x}, \dots, c_{n,A,q_x}, c_{n,B,q_x}, \dots)^T$, its matrix form is

$$\mathcal{H}_{2,1} = \tau_0 \otimes s_z \otimes \begin{pmatrix} 2\sqrt{3}\lambda_{so}q_x & 0 & -\sqrt{3}\lambda_{so}q_x & 0 & 0 & 0 & \cdots \\ 0 & -2\sqrt{3}\lambda_{so}q_x & 0 & \sqrt{3}\lambda_{so}q_x & 0 & 0 & \cdots \\ -\sqrt{3}\lambda_{so}q_x & 0 & 2\sqrt{3}\lambda_{so}q_x & 0 & -\sqrt{3}\lambda_{so}q_x & 0 & \cdots \\ 0 & \sqrt{3}\lambda_{so}q_x & 0 & -2\sqrt{3}\lambda_{so}q_x & 0 & \sqrt{3}\lambda_{so}q_x & \cdots \\ 0 & 0 & -\sqrt{3}\lambda_{so}q_x & 0 & 2\sqrt{3}\lambda_{so}q_x & 0 & \cdots \\ 0 & 0 & 0 & \sqrt{3}\lambda_{so}q_x & 0 & -2\sqrt{3}\lambda_{so}q_x & \cdots \\ \vdots & \vdots & \vdots & \vdots & \vdots & \vdots & \ddots \end{pmatrix}. \quad (\text{S10})$$

Then the contribution from $\mathcal{H}_{2,1}$ to the boundary Hamiltonian is

$$\begin{aligned}
(\mathcal{H}_{beard,1})_{\tau s, \tau' s'} &= \langle \Psi_{\tau s} | \mathcal{H}_{2,1} | \Psi_{\tau' s'} \rangle \\
&= 2\sqrt{3}\lambda_{so,s}q_x\delta_{\tau\tau'}\delta_{ss'} - \sqrt{3}\lambda_{so,s}q_x\delta_{\tau\tau'}\delta_{ss'}\mathcal{N}^2\sum_{n=1}^{+\infty}2\psi_{nA}\psi_{(n+1)A} \\
&= 2\sqrt{3}\lambda_{so,s}q_x\delta_{\tau\tau'}\delta_{ss'} + \sqrt{3}\lambda_{so,s}q_x\delta_{\tau\tau'}\delta_{ss'}\mathcal{N}^2\sum_{n=1}^{+\infty}\psi_{nA}\psi_{nA} \\
&= 2\sqrt{3}\lambda_{so,s}q_x\delta_{\tau\tau'}\delta_{ss'} + \sqrt{3}\lambda_{so,s}q_x\delta_{\tau\tau'}\delta_{ss'} \\
&= 3\sqrt{3}\lambda_{so,s}q_x\delta_{\tau\tau'}\delta_{ss'}, \tag{S11}
\end{aligned}$$

where $\lambda_{so,s} \equiv \lambda_{so} s$. In the derivation above, a few facts have been used, including: (1) ψ_{nA} is real; (2) $\psi_{(n+1)A} = -\frac{1}{2}\psi_{nA}$; (3) $\mathcal{N}^2\sum_{n=1}^{+\infty}\psi_{nA}^2 = 1$. Choosing the basis spanning the subspace for boundary Hamiltonian to be $(|\Psi_{11}\rangle, |\Psi_{1-1}\rangle, |\Psi_{-11}\rangle, |\Psi_{-1-1}\rangle)^T$, $\mathcal{H}_{beard,1}$ can be expressed in terms of the Pauli matrices as

$$\mathcal{H}_{beard,1} = 3\sqrt{3}\lambda_{so}q_x\tau_0s_z. \tag{S12}$$

For the second term $\mathcal{H}_{2,2} = -\mu\tau_zs_0\sigma_0$, as it is diagonal in the basis Ψ_{q_x} , one can easily find that its contribution to the boundary Hamiltonian is just

$$\mathcal{H}_{beard,2} = -\mu\tau_zs_0. \tag{S13}$$

Now let us analyze the contribution from the pairing term. In the basis Ψ_{q_x} , the matrix form of the pairing term is

$$\mathcal{H}_{2,3} = - \begin{pmatrix} (\Delta_0 + 2\Delta_2)\tau_y s_y & 0 & 2\Delta_2\tau_y s_y & 0 & \cdots \\ 0 & (\Delta_0 + 2\Delta_2)\tau_y s_y & 0 & 2\Delta_2\tau_y s_y & \cdots \\ 2\Delta_2\tau_y s_y & 0 & (\Delta_0 + 2\Delta_2)\tau_y s_y & 0 & \cdots \\ 0 & 2\Delta_2\tau_y s_y & 0 & (\Delta_0 + 2\Delta_2)\tau_y s_y & \cdots \\ \vdots & \vdots & \vdots & \vdots & \ddots \end{pmatrix}. \tag{S14}$$

Similarly, its contribution to the boundary Hamiltonian is

$$\begin{aligned}
(\mathcal{H}_{beard,3})_{\tau s, \tau' s'} &= \langle \Psi_{\tau s} | \mathcal{H}_{2,3} | \Psi_{\tau' s'} \rangle \\
&= -(\Delta_0 + 2\Delta_2)(\tau_y)_{\tau\tau'}(s_y)_{ss'} - 2\Delta_2(\tau_y)_{\tau\tau'}(s_y)_{ss'}\mathcal{N}^2\sum_{n=1}^{+\infty}2\psi_{nA}\psi_{(n+1)A} \\
&= -(\Delta_0 + 2\Delta_2)(\tau_y)_{\tau\tau'}(s_y)_{ss'} + 2\Delta_2(\tau_y)_{\tau\tau'}(s_y)_{ss'} \\
&= -\Delta_0(\tau_y)_{\tau\tau'}(s_y)_{ss'}. \tag{S15}
\end{aligned}$$

One finds that the contribution from the next-nearest-neighbor pairing will vanish for the beard edge, in agreement with the numerical results shown in Fig.2 of the main text. In terms of the Pauli matrices, its form is just

$$\mathcal{H}_{beard,3} = -\Delta_0\tau_y s_y. \tag{S16}$$

Taking all contributions together, we reach the final expression of the boundary Hamiltonian for the upper beard edge, which reads

$$\mathcal{H}_{beard} = \mathcal{H}_{beard,1} + \mathcal{H}_{beard,2} + \mathcal{H}_{beard,3} = vq_x\tau_0s_z - \mu\tau_zs_0 - \Delta_0\tau_y s_y, \tag{S17}$$

where $v = 3\sqrt{3}\lambda_{so}$. In the limit $\mu = 0$, the boundary Hamiltonian reduces to the form of Eq.(8) in the main text. We find that the boundary energy gap at $k_x = 0$ predicted by the low-energy boundary Hamiltonian agree perfectly with the numerical results when only the on-site pairing or the next-nearest-neighbor pairing is present. When both the on-site and the next-nearest-neighbor pairings are finite, the boundary energy gap is found to be a little smaller than the predicted value $E_g = 2|\Delta_0|$, but the agreement is still very good at the neighborhood of the boundary Dirac point.

B. Low-energy boundary Hamiltonian for the zigzag edge

When the upper edge changes to terminate at type-B sublattices, so a zigzag edge, numerical results show that the boundary Dirac point is shifted to $k_x = \pi/\sqrt{3}$. In order to analytically derive the corresponding boundary Hamiltonian, we similarly perform an expansion around $k_x = \pi/\sqrt{3}$ and keep the momentum up to the linear order. Accordingly, the Hamiltonian becomes

$$\begin{aligned} \mathcal{H}_{\text{BdG}}(q'_x, k_y) &= t(-\sqrt{3}q'_x \cos \frac{k_y}{2} + \cos k_y)\tau_z s_0 \sigma_x + t(\sqrt{3}q'_x \sin \frac{k_y}{2} + \sin k_y)\tau_z s_0 \sigma_y \\ &\quad + 2\lambda_{s_0}(-\sqrt{3}q'_x - 2 \cos \frac{3k_y}{2})\tau_0 s_z \sigma_z - \mu\tau_z s_0 \sigma_0 \\ &\quad - [\Delta_0 + 2\Delta_2(-1 - \sqrt{3}q'_x \cos \frac{3k_y}{2})]\tau_y s_y \sigma_0, \end{aligned} \quad (\text{S18})$$

where q'_x denotes a small momentum measured from $k_x = \pi/\sqrt{3}$. Similar to the previous case, we decompose the Hamiltonian into two parts, $\mathcal{H} = \mathcal{H}_1 + \mathcal{H}_2$, with

$$\begin{aligned} \mathcal{H}_1(q'_x, k_y) &= t \cos k_y \tau_z s_0 \sigma_x + t \sin k_y \tau_z s_0 \sigma_y - 4\lambda_{s_0} \cos \frac{3k_y}{2} \tau_0 s_z \sigma_z, \\ \mathcal{H}_2(q'_x, k_y) &= -\sqrt{3}tq'_x \cos \frac{k_y}{2} \tau_z s_0 \sigma_x + \sqrt{3}tq'_x \sin \frac{k_y}{2} \tau_z s_0 \sigma_y \\ &\quad - 2\sqrt{3}\lambda_{s_0}q'_x \tau_0 s_z \sigma_z - \mu\tau_z s_0 \sigma_0 \\ &\quad - [\Delta_0 + 2\Delta_2(-1 - \sqrt{3}q'_x \cos \frac{3k_y}{2})]\tau_y s_y \sigma_0. \end{aligned} \quad (\text{S19})$$

As we are interested in the small q'_x regime, it is also justified to treat the whole \mathcal{H}_2 as a perturbation.

When the upper edge becomes a zigzag one, the terminating sublattices become type B, so the corresponding basis for a half-infinity system becomes $\Psi_{q'_x} = (c_{1,B,q'_x}, c_{2,A,q'_x}, c_{2,B,q'_x}, c_{3,A,q'_x}, c_{3,B,q'_x}, \dots, c_{n,A,q'_x}, c_{n,B,q'_x}, \dots)^T$. Then \mathcal{H}_1 in matrix form reads

$$\mathcal{H}_1 = \begin{pmatrix} 0 & 0 & 2\lambda_{s_0}\tau_0 s_z & 0 & 0 & 0 & \cdots \\ 0 & 0 & t\tau_z s_0 & -2\lambda_{s_0}\tau_0 s_z & 0 & 0 & \cdots \\ 2\lambda_{s_0}\tau_0 s_z & t\tau_z s_0 & 0 & 0 & 2\lambda_{s_0}\tau_0 s_z & 0 & \cdots \\ 0 & -2\lambda_{s_0}\tau_0 s_z & 0 & 0 & t\tau_z s_0 & -2\lambda_{s_0}\tau_0 s_z & \cdots \\ 0 & 0 & 2\lambda_{s_0}\tau_0 s_z & t\tau_z s_0 & 0 & 0 & \cdots \\ 0 & 0 & 0 & -2\lambda_{s_0}\tau_0 s_z & 0 & 0 & \cdots \\ \vdots & \vdots & \vdots & \vdots & \vdots & \vdots & \ddots \end{pmatrix}, \quad (\text{S20})$$

As τ_z and s_z also commute with \mathcal{H}_1 , the zero-energy eigenvectors of \mathcal{H}_1 can also be assigned the form

$$|\Psi_{\tau s}\rangle = |\tau_z = \tau\rangle \otimes |s_z = s\rangle \otimes (\psi_{1B}, \psi_{2A}, \psi_{2B}, \psi_{3A}, \psi_{3B}, \dots, \psi_{nA}, \psi_{nB}, \dots)^T. \quad (\text{S21})$$

Accordingly, the eigenvalue equation $\mathcal{H}_1|\Psi_{\tau s}\rangle = 0$ leads to the following equations with periodic structures,

$$\begin{aligned} 2\lambda_{s_0,s}\psi_{2B} &= 0, \\ t\tau\psi_{2B} - 2\lambda_{s_0,s}\psi_{3A} &= 0, \\ 2\lambda_{s_0,s}\psi_{1B} + t\tau\psi_{2A} + 2\lambda_{s_0,s}\psi_{3B} &= 0, \\ -2\lambda_{s_0,s}\psi_{2A} + t\tau\psi_{3B} - 2\lambda_{s_0,s}\psi_{4A} &= 0, \\ \dots & \\ 2\lambda_{s_0,s}\psi_{(n-1)B} + t\tau\psi_{nA} + 2\lambda_{s_0,s}\psi_{(n+1)B} &= 0, \\ -2\lambda_{s_0,s}\psi_{nA} + t\tau\psi_{(n+1)B} - 2\lambda_{s_0,s}\psi_{(n+2)A} &= 0, \\ \dots & \end{aligned} \quad (\text{S22})$$

It is readily found that the components of eigenvectors have $\psi_{(2n)B} = \psi_{(2n+1)A} = 0$. Therefore, we only need to focus on the following equations,

$$\begin{aligned} 2\lambda_{s_0,s}\psi_{(2n-1)B} + t\tau\psi_{(2n)A} + 2\lambda_{s_0,s}\psi_{(2n+1)B} &= 0, \\ -2\lambda_{s_0,s}\psi_{(2n)A} + t\tau\psi_{(2n+1)B} - 2\lambda_{s_0,s}\psi_{(2n+2)A} &= 0. \end{aligned} \quad (\text{S23})$$

Consider the trial function

$$\begin{pmatrix} \psi_{(2n+1)B} \\ \psi_{(2n+2)A} \end{pmatrix} = \xi^n \begin{pmatrix} \psi_{1B} \\ \psi_{2A} \end{pmatrix}, \quad (\text{S24})$$

where $|\xi| < 1$ is required so that the wave function decays in real space and corresponds to a bound state. Accordingly, one finds that the series of equations reduce to two algebra equations, which read

$$\begin{aligned} 2\lambda_{s_0,s}\psi_{1B} + t_\tau\psi_{2A} + 2\lambda_{s_0,s}\xi\psi_{1B} &= 0, \\ -2\lambda_{s_0,s}\psi_{2A} + t_\tau\xi\psi_{1B} - 2\lambda_{s_0,s}\xi\psi_{2A} &= 0. \end{aligned} \quad (\text{S25})$$

By simple algebra, one finds

$$\begin{aligned} \psi_{1B} &= -\frac{t_\tau}{2\lambda_{s_0,s}(1+\xi)}\psi_{2A}, \\ \frac{2\lambda_{s_0,s}(1+\xi)}{t_\tau\xi} &= -\frac{t_\tau}{2\lambda_{s_0,s}(1+\xi)}. \end{aligned} \quad (\text{S26})$$

There are two solutions for ξ ,

$$\xi_{\pm} = \frac{-(t_\tau^2 + 8\lambda_{s_0,s}^2) \pm \sqrt{t_\tau^2(t_\tau^2 + 16\lambda_{s_0,s}^2)}}{8\lambda_{s_0,s}^2}, \quad (\text{S27})$$

however, only ξ_+ leads to decaying wave functions, so bound states. Taking ξ_+ back into Eq.(S26), one finds

$$\psi_{1B} = \frac{4t_\tau\lambda_{s_0,s}^2}{\lambda_{s_0,s}(t_\tau^2 - \sqrt{t_\tau^2(t_\tau^2 + 16\lambda_{s_0,s}^2)})}\psi_{2A} \equiv \eta_{\tau s}\psi_{2A} = -\tau s|\eta_{\tau s}| \psi_{2A}. \quad (\text{S28})$$

As τ and s have four possible combinations, there are also four eigenvectors corresponding to four zero-energy bound states. The eigenvectors can also be expressed as

$$|\Psi_{\tau s}\rangle = |\tau_z = \tau\rangle \otimes |s_z = s\rangle \otimes \mathcal{N}(\eta_{\tau s}, 1, 0, 0, \xi_+ \eta_{\tau s}, \xi_+, 0, 0, \xi_+^2 \eta_{\tau s}, \xi_+^2, \dots)^T. \quad (\text{S29})$$

The normalization condition $\langle \Psi_{\tau s} | \Psi_{\tau s} \rangle = 1$ gives

$$\mathcal{N}^2(1 + \eta_{\tau s}^2) \sum_{n=0}^{\infty} \xi_+^{2n} = \mathcal{N}^2 \frac{(1 + \eta_{\tau s}^2)}{1 - \xi_+^2} = 1, \quad (\text{S30})$$

which indicates

$$\mathcal{N} = \sqrt{\frac{1 - \xi_+^2}{1 + \eta_{\tau s}^2}}. \quad (\text{S31})$$

Let us now analyze the effect of \mathcal{H}_2 . For the first two terms in \mathcal{H}_2 , $\mathcal{H}_{2,1+2} = -\sqrt{3}t'_x \cos \frac{k_y}{2} \tau_z s_0 \sigma_x + \sqrt{3}t'_x \sin \frac{k_y}{2} \tau_z s_0 \sigma_y$, the corresponding matrix form reads

$$\mathcal{H}_{2,1+2} = \begin{pmatrix} 0 & -\sqrt{3}t'_x \tau_z s_0 & 0 & 0 & 0 & 0 & \dots \\ -\sqrt{3}t'_x \tau_z s_0 & 0 & 0 & 0 & 0 & 0 & \dots \\ 0 & 0 & 0 & -\sqrt{3}t'_x \tau_z s_0 & 0 & 0 & \dots \\ 0 & 0 & -\sqrt{3}t'_x \tau_z s_0 & 0 & 0 & 0 & \dots \\ 0 & 0 & 0 & 0 & 0 & -\sqrt{3}t'_x \tau_z s_0 & \dots \\ 0 & 0 & 0 & 0 & -\sqrt{3}t'_x \tau_z s_0 & 0 & \dots \\ \vdots & \vdots & \vdots & \vdots & \vdots & \vdots & \ddots \end{pmatrix}. \quad (\text{S32})$$

By projecting $\mathcal{H}_{2,1+2}$ onto $\{|\Psi_{\tau s}\rangle\}$, one finds its contribution to the boundary Hamiltonian, which reads

$$\begin{aligned} (\mathcal{H}_{zigzag,1})_{\tau s, \tau' s'} &= \langle \Psi_{\tau s}^\dagger | \mathcal{H}_{2,1+2} | \Psi_{\tau' s'} \rangle \\ &= -2\sqrt{3}t'_x \tau \eta_{\tau s} \delta_{\tau \tau'} \delta_{s s'} \mathcal{N}^2 \sum_{n=0}^{\infty} \xi_+^{2n} \\ &= -\frac{2\sqrt{3}t'_x \tau \eta_{\tau s}}{1 + \eta_{\tau s}^2} q'_x \delta_{\tau \tau'} \delta_{s s'} \\ &= \frac{2\sqrt{3}t'_x |\eta_{\tau s}|}{1 + \eta_{\tau s}^2} s q'_x \delta_{\tau \tau'} \delta_{s s'}. \end{aligned} \quad (\text{S33})$$

Above in the last step, we have used the facts $\eta_{\tau s} = -\tau s |\eta_{\tau s}|$ and $\tau^2 = 1$. Also choosing the basis to be $(|\Psi_{11}\rangle, |\Psi_{1-1}\rangle, |\Psi_{-11}\rangle, |\Psi_{-1-1}\rangle)^T$, then $\mathcal{H}_{zigzag,1}$ can be expressed in terms of the Pauli matrices as

$$\mathcal{H}_{zigzag,1} = \frac{2\sqrt{3}t|\eta_{\tau s}|}{1 + \eta_{\tau s}^2} q'_x \tau_0 s_z. \quad (\text{S34})$$

For the third term, $\mathcal{H}_{2,3} = -2\sqrt{3}\lambda_{so}q'_x\tau_0s_z\sigma_z$, its matrix form reads

$$\mathcal{H}_{2,3} = \tau_0 \otimes s_z \otimes \begin{pmatrix} 2\sqrt{3}\lambda_{so}q'_x & 0 & 0 & 0 & 0 & 0 & \cdots \\ 0 & -2\sqrt{3}\lambda_{so}q'_x & 0 & 0 & 0 & 0 & \cdots \\ 0 & 0 & 2\sqrt{3}\lambda_{so}q'_x & 0 & 0 & 0 & \cdots \\ 0 & 0 & 0 & -2\sqrt{3}\lambda_{so}q'_x & 0 & 0 & \cdots \\ 0 & 0 & 0 & 0 & 2\sqrt{3}\lambda_{so}q'_x & 0 & \cdots \\ 0 & 0 & 0 & 0 & 0 & -2\sqrt{3}\lambda_{so}q'_x & \cdots \\ \vdots & \vdots & \vdots & \vdots & \vdots & \vdots & \ddots \end{pmatrix}. \quad (\text{S35})$$

Its contribution to the boundary Hamiltonian can be similarly determined, which takes the form

$$\begin{aligned} (\mathcal{H}_{zigzag,2})_{\tau s, \tau' s'} &= \langle \Psi_{\tau s}^\dagger | \mathcal{H}_{2,3} | \Psi_{\tau' s'} \rangle \\ &= 2\sqrt{3}\lambda_{so}s q'_x (\eta_{\tau s}^2 - 1) \mathcal{N}^2 \sum_{n=0}^{\infty} \xi_+^{2n} \delta_{\tau\tau'} \delta_{ss'} \\ &= \frac{2\sqrt{3}\lambda_{so}(\eta_{\tau s}^2 - 1)s}{1 + \eta_{\tau s}^2} q'_x \delta_{\tau\tau'} \delta_{ss'}. \end{aligned} \quad (\text{S36})$$

Also in terms of the Pauli matrices, its form can be expressed as

$$\mathcal{H}_{zigzag,2} = \frac{2\sqrt{3}\lambda_{so}(\eta_{\tau s}^2 - 1)}{1 + \eta_{\tau s}^2} q'_x \tau_0 s_z. \quad (\text{S37})$$

A combination of the two contributions gives the full expression for the linear momentum term in the boundary Dirac Hamiltonian. For the chemical potential term, its contribution is also simply

$$\mathcal{H}_{zigzag,3} = -\mu\tau_z s_0. \quad (\text{S38})$$

Let us now analyze the contribution from the last piece, the pairing term $\mathcal{H}_{2,5} = -[\Delta_0 + 2\Delta_2(-1 - \sqrt{3}q'_x \cos \frac{3k_y}{2})]\tau_y s_y \sigma_0$. Its explicit matrix form is

$$\mathcal{H}_{2,5} = \begin{pmatrix} -(\Delta_0 - 2\Delta_2)\tau_y s_y & 0 & \sqrt{3}\Delta_2 q'_x \tau_y s_y & 0 & \cdots \\ 0 & -(\Delta_0 - 2\Delta_2)\tau_y s_y & 0 & \sqrt{3}\Delta_2 q'_x \tau_y s_y & \cdots \\ \sqrt{3}\Delta_2 q'_x \tau_y s_y & 0 & -(\Delta_0 - 2\Delta_2)\tau_y s_y & 0 & \cdots \\ 0 & \sqrt{3}\Delta_2 q'_x \tau_y s_y & 0 & -(\Delta_0 - 2\Delta_2)\tau_y s_y & \cdots \\ \vdots & \vdots & \vdots & \vdots & \ddots \end{pmatrix}. \quad (\text{S39})$$

Its contribution to the boundary Hamiltonian is

$$\begin{aligned} (\mathcal{H}_{zigzag,4})_{\tau s, \tau' s'} &= \langle \Psi_{\tau s} | \mathcal{H}_{2,5} | \Psi_{\tau' s'} \rangle \\ &= -(\Delta_0 - 2\Delta_2)(\tau_y)_{\tau\tau'} (s_y)_{ss'} + \sqrt{3}\Delta_2 q'_x (\tau_y)_{\tau\tau'} (s_y)_{ss'} \mathcal{N}^2 \sum_{n=1}^{+\infty} 2[\psi_{nB}\psi_{(n+1)B} + \psi_{(n+1)A}\psi_{(n+2)A}] \\ &= -(\Delta_0 - 2\Delta_2)(\tau_y)_{\tau\tau'} (s_y)_{ss'}. \end{aligned} \quad (\text{S40})$$

In the last step, we have used the fact that the products $\psi_{nB}\psi_{(n+1)B}$ and $\psi_{nA}\psi_{(n+1)A}$ are always zero as $\psi_{(2n+1)A} = \psi_{2nB} = 0$. In terms of the Pauli matrices,

$$\mathcal{H}_{zigzag,4} = -(\Delta_0 - 2\Delta_2)\tau_y s_y. \quad (\text{S41})$$

Taking all contribution together, we reach the final expression for the boundary Hamiltonian for the upper zigzag edge, which reads

$$\mathcal{H}_{zigzag} = \sum_{i=1}^4 \mathcal{H}_{zigzag,i} = v' q'_x \tau_0 s_z - \mu\tau_z s_0 - (\Delta_0 - 2\Delta_2)\tau_y s_y, \quad (\text{S42})$$

where

$$v' = \left[\frac{2\sqrt{3}t|\eta_{\tau s}| + 2\sqrt{3}\lambda_{so}(\eta_{\tau s}^2 - 1)}{1 + \eta_{\tau s}^2} \right]. \quad (\text{S43})$$

When $\lambda_{so} \ll t$, one can do an expansion of $\eta_{\tau s}$ about λ_{so}/t . Only keeping the leading-order term, the result is

$$\begin{aligned} |\eta_{\tau,s}| &= \frac{4t\lambda_{so}^2}{\lambda_{so}(\sqrt{t^2(t^2 + 16\lambda_{so}^2)} - t^2)} \\ &\approx \frac{4t\lambda_{so}^2}{\lambda_{so}(t^2 + 8\lambda_{so}^2 - t^2)} \\ &= \frac{t}{2\lambda_{so}}. \end{aligned} \quad (\text{S44})$$

When $\lambda_{so} \ll t$, $|\eta_{\tau,s}| \gg 1$, so $\eta_{\tau s}^2 \pm 1 \approx \eta_{\tau s}^2$, one finds

$$\begin{aligned} v' &= \frac{2\sqrt{3}t|\eta_{\tau s}| + 2\sqrt{3}\lambda_{so}(\eta_{\tau s}^2 - 1)}{1 + \eta_{\tau s}^2} \\ &\approx \frac{2\sqrt{3}t|\eta_{\tau s}| + 2\sqrt{3}\lambda_{so}\eta_{\tau s}^2}{\eta_{\tau s}^2} \\ &\approx 6\sqrt{3}\lambda_{so}. \end{aligned} \quad (\text{S45})$$

In the limit $\mu = 0$, the boundary Hamiltonian reduces to the form of Eq.(9) in the main text. By comparing the analytical results with the numerical results, we find that the above low-energy boundary Hamiltonian gives a very accurate description of the physics on the zigzag edge.

II. TWO-DIMENSIONAL HONEYCOMB-LATTICE TOPOLOGICAL INSULATORS IN PROXIMITY TO D-WAVE SUPERCONDUCTORS

In the main text, we have used the isotropic extended s-wave pairing to illustrate the physics. To show explicitly that the physics does not rely on a specific pairing type, in this section we consider the d-wave pairing, a pairing type widely believed to be relevant to high- T_c cuprate-based superconductors. On a honeycomb lattice, the pairing amplitude of the d-wave pairing follows the pattern $\Delta_{\alpha,ij} = \Delta_\alpha \cos 2\theta_{ij}$, with θ_{ij} denoting the angle that the bond vector \mathbf{d}_{ij} is in regard to the x direction. Accordingly, the Kane-Mele model with d-wave pairing up to the next-nearest neighbors reads

$$\begin{aligned} \mathcal{H}_{\text{BdG}}(\mathbf{k}) &= t(2 \cos \frac{\sqrt{3}k_x}{2} \cos \frac{k_y}{2} + \cos k_y)\tau_z s_0 \sigma_x - t(2 \cos \frac{\sqrt{3}k_x}{2} \sin \frac{k_y}{2} - \sin k_y)\tau_z s_0 \sigma_y \\ &\quad + 2\lambda_{so}(\sin \sqrt{3}k_x - 2 \sin \frac{\sqrt{3}k_x}{2} \cos \frac{3k_y}{2})\tau_0 s_z \sigma_z - \mu\tau_z s_0 \sigma_0 \\ &\quad - \Delta_1(\cos \frac{\sqrt{3}k_x}{2} \cos \frac{k_y}{2} - \cos k_y)\tau_y s_y \sigma_x + \Delta_1(\cos \frac{\sqrt{3}k_x}{2} \sin \frac{k_y}{2} + \sin k_y)\tau_y s_y \sigma_y \\ &\quad - 2\Delta_2(\cos \sqrt{3}k_x - \cos \frac{\sqrt{3}k_x}{2} \cos \frac{3k_y}{2})\tau_y s_y \sigma_0. \end{aligned} \quad (\text{S46})$$

Similar to the extended s-wave pairing, we find that the nearest-neighbor pairing also has a negligible effect to the helical edge states, and only the next-nearest-neighbor pairing can open a gap to the boundary Dirac points, as shown in Fig.S1. Therefore, below we also set $\Delta_1 = 0$ for simplicity. In parallel to the extended s-wave pairing case, we first derive the corresponding low-energy boundary Hamiltonian for both beard and zigzag edges, and then numerically show the realization of Majorana Kramers pairs at the sublattice domain walls once the topological criterion is fulfilled.

A. Low-energy boundary Hamiltonian for the beard edge

Compared to the extended s-wave pairing case, since only the pairing term has been changed, what we need to concern is just the change of Dirac mass. For the beard edge, as aforementioned the expansion of the Hamiltonian is around $k_x = 0$. Also only

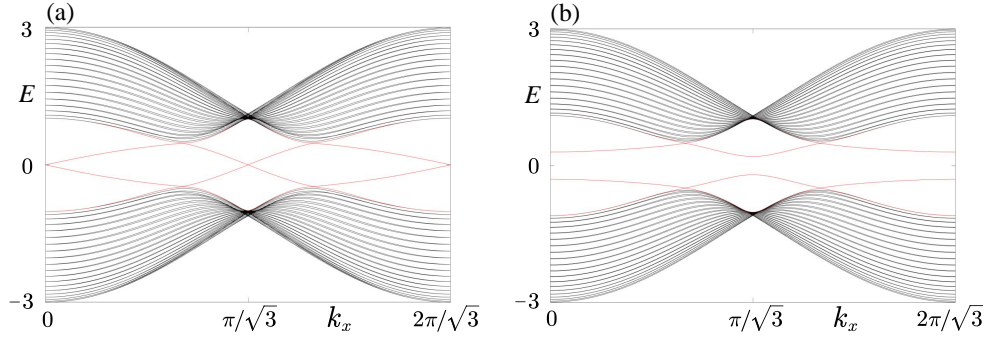


FIG. S1. (Color online) Energy spectrum for the Kane-Mele model with d-wave pairing. A cylindrical geometry is considered, with periodic boundary condition in the x direction and open boundary condition in the y direction. The upper y -normal boundary is a beard edge, and the lower y -normal boundary is a zigzag edge. In (a) and (b), $t = 1$, $\lambda_{so} = 0.1$, $\mu = 0$. In (a), $\Delta_1 = 0.1$ and $\Delta_2 = 0$, the boundary Dirac points at time-reversal invariant momenta turn out to be robust against the nearest-neighbor pairing. In (b), $\Delta_1 = 0$ and $\Delta_2 = 0.1$, the boundary Dirac points are gapped by the next-nearest-neighbor pairing.

remaining terms up to the linear order in momentum, the Hamiltonian reads

$$\begin{aligned} \mathcal{H}_{\text{BdG}}(q_x, k_y) = & t(2 \cos \frac{k_y}{2} + \cos k_y) \tau_z s_0 \sigma_x - t(2 \sin \frac{k_y}{2} - \sin k_y) \tau_z s_0 \sigma_y \\ & + 2\sqrt{3} \lambda_{so} q_x (1 - \cos \frac{3k_y}{2}) \tau_0 s_z \sigma_z - \mu \tau_z s_0 \sigma_0 \\ & - 2\Delta_2 (1 - \cos \frac{3k_y}{2}) \tau_y s_y \sigma_0, \end{aligned} \quad (\text{S47})$$

where the last line corresponds to the pairing term at the neighborhood of $k_x = 0$. Focusing on the last line, its matrix form in the underlying basis $\Psi_{q_x} = (c_{1,A,q_x}, c_{1,B,q_x}, c_{2,A,q_x}, c_{2,B,q_x}, \dots, c_{n,A,q_x}, c_{n,B,q_x}, \dots)^T$ is

$$\mathcal{H}_{dSC} = \begin{pmatrix} -2\Delta_2 \tau_y s_y & 0 & \Delta_2 \tau_y s_y & 0 & \dots \\ 0 & -2\Delta_2 \tau_y s_y & 0 & \Delta_2 \tau_y s_y & \dots \\ \Delta_2 \tau_y s_y & 0 & -2\Delta_2 \tau_y s_y & 0 & \dots \\ 0 & \Delta_2 \tau_y s_y & 0 & -2\Delta_2 \tau_y s_y & \dots \\ \vdots & \vdots & \vdots & \vdots & \ddots \end{pmatrix}. \quad (\text{S48})$$

Also taking this term as a perturbation and projecting it onto the subspace spanned by the four eigenvectors $|\Psi_{\tau s}\rangle$, where

$$|\Psi_{\tau s}\rangle = |\tau_z = \tau\rangle \otimes |s_z = s\rangle \otimes \frac{\sqrt{3}}{2} (1, 0, -\frac{1}{2}, 0, \dots, (-\frac{1}{2})^{(n-1)}, 0, \dots)^T, \quad (\text{S49})$$

one finds that its contribution is

$$\begin{aligned} (\mathcal{H}_{\text{beard},3})_{\tau s, \tau' s'} &= \langle \Psi_{\tau s} | \mathcal{H}_{dSC} | \Psi_{\tau' s'} \rangle \\ &= -2\Delta_2 (\tau_y)_{\tau \tau'} (s_y)_{ss'} - \Delta_2 (\tau_y)_{\tau \tau'} (s_y)_{ss'} \\ &= -3\Delta_2 (\tau_y)_{\tau \tau'} (s_y)_{ss'}. \end{aligned} \quad (\text{S50})$$

In terms of the Pauli matrices, its form is

$$\mathcal{H}_{\text{beard},3} = -3\Delta_2 \tau_y s_y. \quad (\text{S51})$$

Replacing the Dirac mass term in Eq.(S17) by the above Dirac mass term, one gets

$$\mathcal{H}_{\text{beard}} = v q_x \tau_0 s_z - \mu \tau_z s_0 - 3\Delta_2 \tau_y s_y. \quad (\text{S52})$$

This is the low-energy boundary Hamiltonian for the beard edge when the pairing is d-wave type.

B. Low-energy boundary Hamiltonian for the zigzag edge

For zigzag edge and d-wave pairing, an expansion of the Hamiltonian around $k_x = \pi/\sqrt{3}$ up to the linear order in momentum gives

$$\begin{aligned} \mathcal{H}_{\text{BdG}}(q'_x, k_y) &= t(-\sqrt{3}q'_x \cos \frac{k_y}{2} + \cos k_y)\tau_z s_0 \sigma_x + t(\sqrt{3}q'_x \sin \frac{k_y}{2} + \sin k_y)\tau_z s_0 \sigma_y \\ &\quad + 2\lambda_{s_0}(-\sqrt{3}q'_x - 2 \cos \frac{3k_y}{2})\tau_0 s_z \sigma_z - \mu\tau_z s_0 \sigma_0 \\ &\quad - 2\Delta_2(-1 + \frac{\sqrt{3}}{2}q'_x \cos \frac{3k_y}{2})\tau_y s_y \sigma_0. \end{aligned} \quad (\text{S53})$$

where the last line corresponds to the pairing term at the neighborhood of $k_x = \pi/\sqrt{3}$.

In the basis $\Psi_{q'_x} = (c_{1,B,q'_x}, c_{2,A,q'_x}, c_{2,B,q'_x}, c_{3,A,q'_x}, c_{3,B,q'_x}, \dots, c_{n,A,q'_x}, c_{n,B,q'_x}, \dots)^T$, the matrix form of the pairing term reads

$$\mathcal{H}_{dSC} = \begin{pmatrix} 2\Delta_2\tau_y s_y & 0 & -\frac{\sqrt{3}}{2}\Delta_2q'_x\tau_y s_y & 0 & \dots \\ 0 & 2\Delta_2\tau_y s_y & 0 & -\frac{\sqrt{3}}{2}\Delta_2q'_x\tau_y s_y & \dots \\ -\frac{\sqrt{3}}{2}\Delta_2q'_x\tau_y s_y & 0 & 2\Delta_2\tau_y s_y & 0 & \dots \\ 0 & -\frac{\sqrt{3}}{2}\Delta_2q'_x\tau_y s_y & 0 & 2\Delta_2\tau_y s_y & \dots \\ \vdots & \vdots & \vdots & \vdots & \ddots \end{pmatrix}. \quad (\text{S54})$$

Also taking this term as a perturbation and projecting it onto the subspace spanned by the four eigenvectors $|\Psi_{\tau s}\rangle$, where

$$|\Psi_{\tau s}\rangle = |\tau_z = \tau\rangle \otimes |s_z = s\rangle \otimes \mathcal{N}(\eta_{\tau s}, 1, 0, 0, \xi_+ \eta_{\tau s}, \xi_+, 0, 0, \xi_+^2 \eta_{\tau s}, \xi_+^2, \dots)^T \quad (\text{S55})$$

with ξ , $\eta_{\tau s}$ and \mathcal{N} given by Eqs.(S27), (S28) and (S31), respectively, one finds that its contribution is

$$\begin{aligned} (\mathcal{H}_{\text{zigzag},5})_{\tau s, \tau' s'} &= \langle \Psi_{\tau s} | \mathcal{H}_{dSC} | \Psi_{\tau' s'} \rangle \\ &= 2\Delta_2(\tau_y)_{\tau\tau'}(s_y)_{s's'}. \end{aligned} \quad (\text{S56})$$

In terms of the Pauli matrices, its form can be expressed as

$$\mathcal{H}_{\text{zigzag},5} = 2\Delta_2\tau_y s_y. \quad (\text{S57})$$

Replacing the Dirac mass term in Eq.(S17) by the above Dirac mass term, one gets

$$\mathcal{H}_{\text{zigzag}} = v'q'_x\tau_0 s_z - \mu\tau_z s_0 + 2\Delta_2\tau_y s_y. \quad (\text{S58})$$

This is the low-energy boundary Hamiltonian for the zigzag edge when the pairing is d-wave type.

C. Majorana Kramers pairs at sublattice domain walls on the upper boundary

Let us focus on the special case with $\mu = 0$. According to the low-energy boundary Hamiltonian for both beard and zigzag edges, one knows that if the upper boundary becomes nonuniform and consists of two parts which respectively terminate at A and B sublattices, the corresponding low-energy boundary Hamiltonian, due to the further breaking of translation symmetry in the x direction, will become

$$\mathcal{H} = -iv(x)\partial_x\tau_0 s_z + m(x)\tau_y s_y, \quad (\text{S59})$$

where $v(x) = v$, $m(x) = -3\Delta_2$ if the part corresponds to a beard edge, and $v(x) = v'$, $m(x) = 2\Delta_2$ if the part corresponds to a zigzag edge. The velocities in both parts have the same sign, but the Dirac masses have opposite signs, as a result, the sublattice domain walls correspond to domain walls of Dirac mass as long as $\Delta_2 \neq 0$. This conclusion suggests that the sublattice domain walls will bind Majorana Kramers pairs if the next-nearest-neighboring pairing is finite. Through numerical calculations, we confirm the appearance of Majorana Kramers pairs at the sublattice domain walls, as shown in Fig.S2. The results in this section demonstrate that the emergence of Majorana zero modes at sublattice domain walls is not restricted to certain specific pairing type.

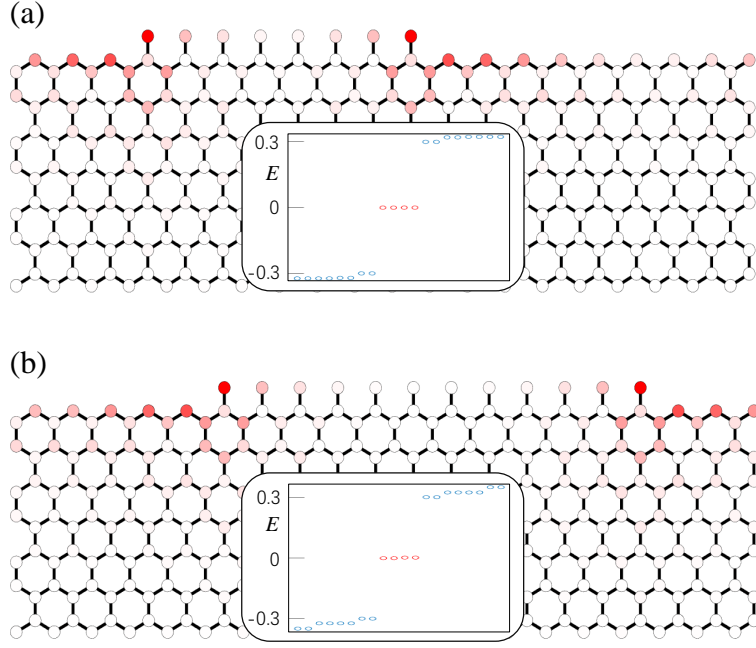


FIG. S2. (Color online) Majorana Kramers pairs at sublattice domain walls on the upper boundary. The lattice geometry is cylindrical with periodic boundary condition in the x direction except for the upper most beard-edge part (left and right edges are considered to be connected in our numerical calculations). Throughout this work, the same boundary conditions are applied to all similar lattice geometries, below the boundary conditions will no longer be emphasized when similar lattice geometries are present. In (a) and (b), $t = 1$, $\lambda_{so} = 0.1$, $\mu = 0$, $\Delta_1 = 0$, $\Delta_2 = 0.15$, and the considered lattice geometry and size are shown explicitly. The insets on top of the underlying lattices correspond to the energy spectra. Here we have only shown the part of eigenvalues closest to zero energy. The middle four dots in red indicate the existence of two Majorana Kramers pairs. The shade of red color on the lattice sites reflect the weight of the probability density ($|\psi(x, y)|^2$) of Majorana Kramers pairs.

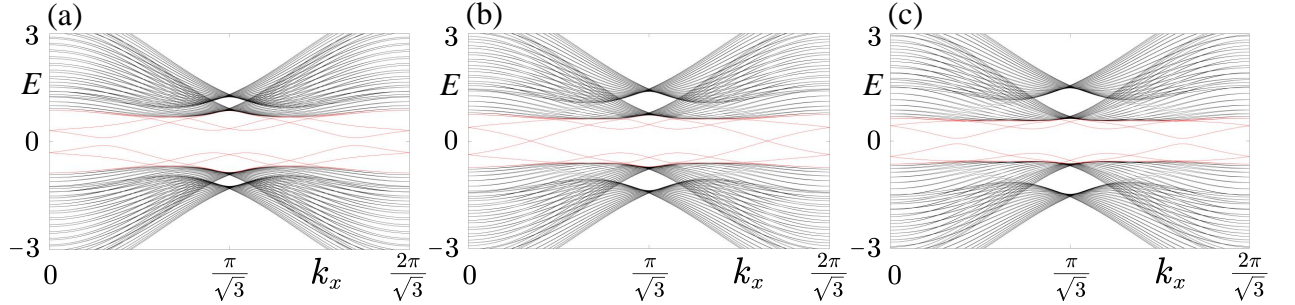


FIG. S3. (Color online) The evolution of boundary energy gap with respect to μ . A cylindrical geometry is considered, with periodic boundary condition in the x direction and open boundary condition in the y direction. The upper y -normal boundary is a beard edge, and the lower y -normal boundary is a zigzag edge. Here the extended s-wave pairing is considered. In (a)-(c), $t = 1$, $\lambda_{so} = 0.1$, $\Delta_0 = \Delta_2 = 0.3$, $\Delta_1 = 0$. (a) $\mu = 0.2$, the mid-gap red lines show the existence of a finite gap in the boundary energy spectrum. (b) $\mu = 0.345$, the boundary energy gap vanishes, corresponding to the critical point of a boundary topological phase transition. (c) $\mu = 0.45$, a gap is reopened in the boundary energy spectrum.

III. THE IMPACT OF FINITE CHEMICAL POTENTIAL ON THE TOPOLOGICAL CRITERION

Above we have restricted to the $\mu = 0$ case for illustration. As the robustness of Majorana Kramers pairs is protected by non-spatial time-reversal symmetry and particle-hole symmetry and the chemical potential term does not break these two symmetries, the Majorana Kramers pairs will remain robust as long as the chemical potential is lower than a critical value. Before proceeding, it is worth noting that in this work we consider that the superconductivity in the two-dimensional topological insulator is induced by proximity effect. Accordingly, the chemical potential is not required to cross the bulk conduction or valence band to guarantee a metallic normal state to achieve superconductivity.

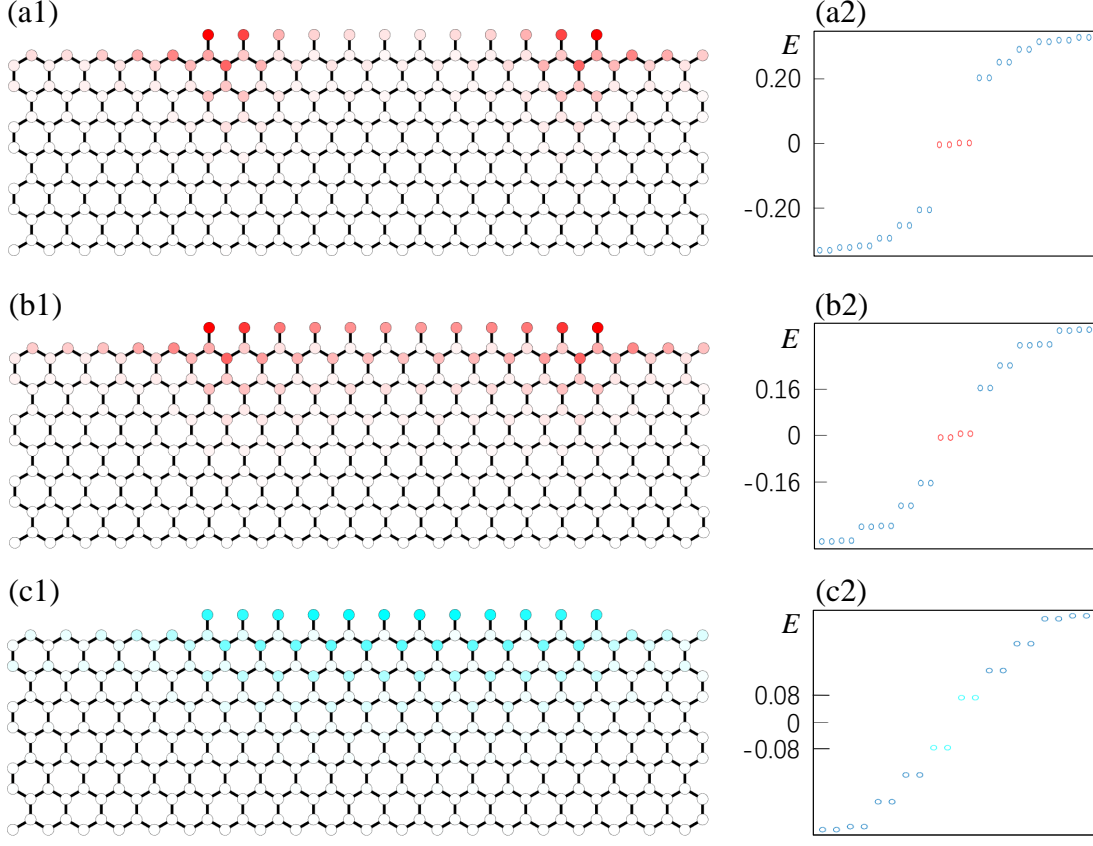


FIG. S4. (Color online) The effect of chemical potential to Majorana Kramer pairs. In (a1)-(c2), $t = 1$, $\lambda_{so} = 0.1$, $\Delta_0 = \Delta_2 = 0.3$, $\Delta_1 = 0$. In (a1) and (a2), $\mu = 0.1$, the wave functions of Majorana Kramer pairs remain well-localized so their energy splitting (see red dots in (a2)) induced by the overlap of wave functions in the considered finite-size system remains small. In (b1) and (b2), $\mu = 0.2$, the increase of μ reduces the boundary energy gap. As a result, the localization of the wave functions of Majorana Kramer pairs becomes relatively poorer and the energy splitting increases due to the finite size of the geometry. In (c1) and (c2), $\mu = 0.4$, no Majorana Kramer pairs are found as the chemical potential is beyond the critical value. The dots in cyan correspond to the lowest-energy excitations. One can see from (c1) that their wave functions are quite uniform on the beard edge of the upper boundary.

Since the Majorana Kramer pairs have codimension $d_c = 2$, the critical chemical potential corresponds to the value at which a boundary topological phase transition occurs. At the critical point of a boundary topological phase transition, the boundary energy gap vanishes, while the bulk energy gap can remain open. We can first give an estimate of the critical value through the low-energy boundary Hamiltonian. According to Eqs.(S17) and (S42), the Dirac mass changes sign from $k_x = 0$ to $k_x = \pi/\sqrt{3}$ when $|\Delta_2| > |\Delta_0|/2 > 0$. It indicates that there exists a node between 0 and $\pi/\sqrt{3}$. Furthermore, as the Δ_2 -term cannot open a gap at $k_x = 0$ and the Δ_0 -term opens an equal gap at $k_x = 0$ and $k_x = \pi/\sqrt{3}$, according to the tight-binding form of the pairing term in Eq.(S1), the Dirac mass induced by the on-site and next-nearest-neighbor pairings on the boundary can be approximated as

$$m(k_x) \approx -\Delta_0 + 2\Delta_2(\cos \sqrt{3}k_x - \cos \frac{\sqrt{3}}{2}k_x). \quad (\text{S60})$$

For the parameters considered in the main text, $\Delta_0 = \Delta_2 = 0.3$, the node determined by the above formula is located at $k_{x,n} \simeq 0.73$. Since this momentum is closer to $k_x = 0$ than to $k_x = \pi/\sqrt{3}$, we can focus on the low-energy boundary Hamiltonian for the beard edge shown in Eq.(S17), whose energy spectrum is

$$E = \pm \sqrt{(3\sqrt{3}\lambda_{so}q_x \pm \mu)^2 + m^2(q_x)}. \quad (\text{S61})$$

Accordingly, the critical chemical potential is approximately given by

$$\mu_c \approx 3\sqrt{3}\lambda_{so}k_{x,n} \simeq 3.8\lambda_{so}. \quad (\text{S62})$$

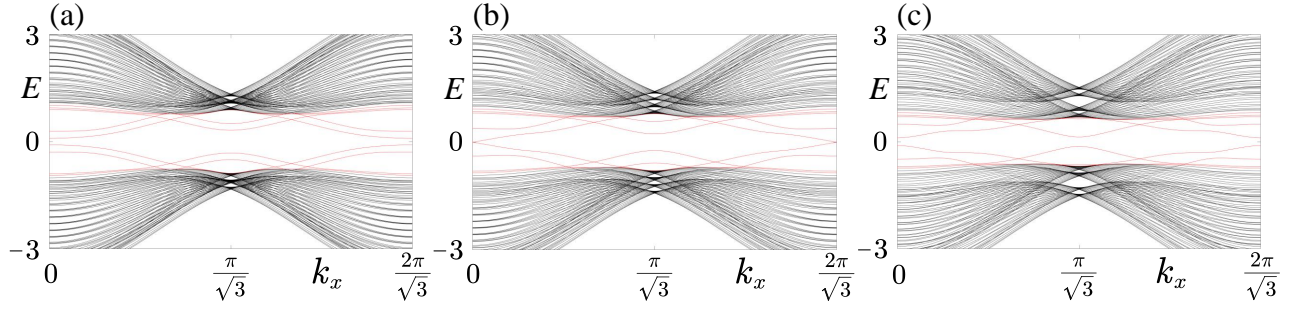


FIG. S5. (Color online) The evolution of boundary energy gap with respect to μ . The lattice geometry is cylindrical with periodic boundary condition in the x direction and open boundary condition in the y direction. The upper y -normal boundary is a beard edge, and the lower y -normal boundary is a zigzag edge. Here the extended s-wave pairing is considered. In (a)-(c), $t = 1$, $\lambda_{so} = 0.1$, $\Delta_0 = 0.2$, $\Delta_2 = 0.3$, $\Delta_1 = 0$. (a) $B_x = 0.1$, the mid-gap red lines show the existence of a finite gap in the boundary energy spectrum. (b) $B_x = 0.191$, the boundary energy gap vanishes, corresponding to the critical point of a boundary topological phase transition. (c) $B_x = 0.3$, a gap is reopened in the boundary energy spectrum.

For $\lambda_{so} = 0.1$, $\mu_c \approx 0.38$. In Fig.S3, the evolution of boundary energy gap with respect to μ is shown. Fig.S3(b) shows that the precise value of μ_c for the given set of parameters is 0.345, quite close to the estimated value. The formula in Eq.(S62) indicates that a stronger spin-orbit coupling admits a larger range of chemical potential within which the sublattice domain walls can host Majorana Kramers pairs.

In Fig.S4, the numerical results confirm that the Majorana Kramers pairs are robust against the increase of chemical potential as long as its value remains lower than the critical value.

IV. SUBLATTICE-SENSITIVE MAJORANA MODES IN TIME-REVERSAL SYMMETRY BROKEN SYSTEMS

So far, we have restricted to time-reversal invariant cases. In this section, we consider the introduction of an in-plane magnetic field to break the time-reversal symmetry. To be specific, we consider that the magnetic field is applied in the x direction, in parallel to the domain walls on the upper boundary. The magnetic field will contribute a Zeeman splitting term of the form $B_x \tau_z s_x \sigma_0$ (g -factor and Bohr magneton are absorbed in B_x for notational simplicity) to the Hamiltonian. Also treating this term as a perturbation, since this term contains σ_0 in the sublattice subspace, one can easily find that it will contribute a Dirac mass term of the form $B_x \tau_z s_x$ for both beard and zigzag edges. For generality, let us assume that the Dirac mass induced by superconductivity on the beard edge is of the form $m_b \tau_y s_y$ and that on the zigzag edge is of the form $m_z \tau_y s_y$. Taking into account the contribution from the Zeeman field, the corresponding low-energy boundary Hamiltonians are

$$\begin{aligned} H_{beard} &= v q_x \tau_0 s_z - \mu \tau_z s_0 + m_b \tau_y s_y + B_x \tau_z s_x, \\ H_{zigzag} &= v' q'_x \tau_0 s_z - \mu \tau_z s_0 + m_z \tau_y s_y + B_x \tau_z s_x. \end{aligned} \quad (\text{S63})$$

Similar to the chemical potential, the Zeeman field will induce a boundary topological phase transition when it induces a gap closure in the boundary energy spectrum. According to the boundary energy spectrum,

$$\begin{aligned} E_{beard}(q_x) &= \pm \sqrt{v^2 q_x^2 + \mu^2 + m_b^2 + B_x^2 \pm 2\sqrt{\mu^2 v^2 q_x^2 + B_x^2 (\mu^2 + m_b^2)}}, \\ E_{zigzag}(q'_x) &= \pm \sqrt{v'^2 q'^2_x + \mu^2 + m_z^2 + B_x^2 \pm 2\sqrt{\mu^2 v'^2 q'^2_x + B_x^2 (\mu^2 + m_z^2)}}. \end{aligned} \quad (\text{S64})$$

For both beard and zigzag edges, the boundary energy gaps will get closed at the time-reversal invariant momentum, i.e., $q_x = 0$, $q'_x = 0$. For the beard edge, the closure of boundary energy gap occurs when $|B_x| = B_{b,c} \equiv \sqrt{\mu^2 + m_b^2}$. For the zigzag edge, the condition is similar, that is, $|B_x| = B_{z,c} \equiv \sqrt{\mu^2 + m_z^2}$. The critical conditions for the two types of edges indicate that if the Zeeman field is chosen to satisfy $\min\{B_{b,c}, B_{z,c}\} < B_x < \max\{B_{b,c}, B_{z,c}\}$, the system will enter a new topological phase on the boundary. For this new topological phase, the Dirac mass of sublattice domain walls will become dominated by Zeeman field on one side and by superconductivity on the other side. Accordingly, one sublattice domain wall will change to host a single Majorana zero mode, instead of a Majorana Kramers pair due to the breaking of time-reversal symmetry.

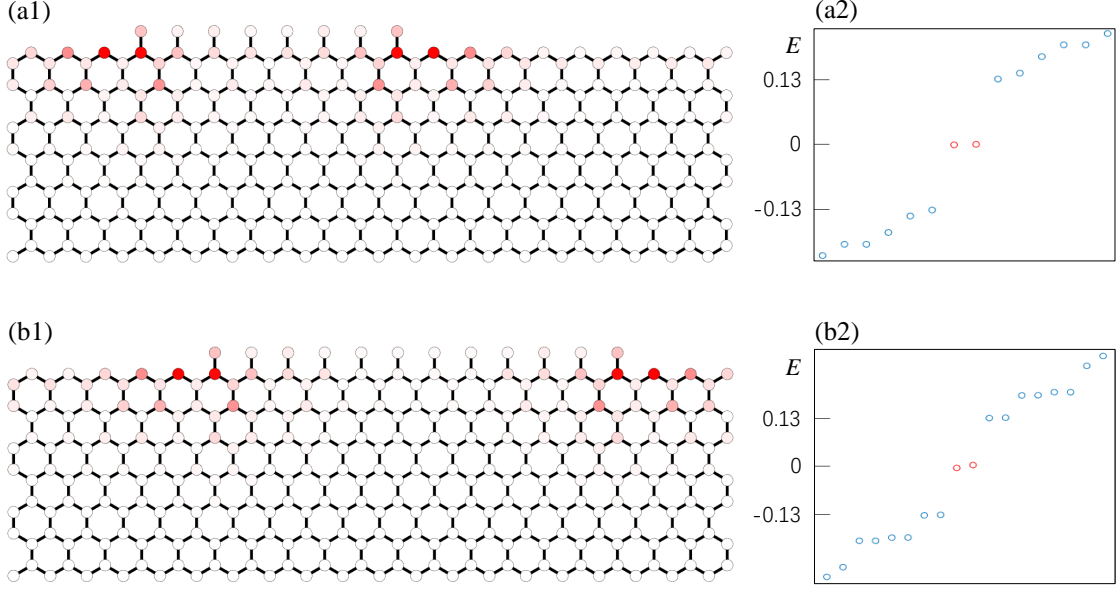


FIG. S6. (Color online) Majorana zero modes at sublattice domain walls. The considered lattice geometry and size are shown explicitly. Here the extended s-wave pairing is considered. In (a1)-(b2), $t = 1$, $\lambda_{so} = 0.1$, $\mu = 0.1$, $\Delta_0 = 0.2$, $\Delta_2 = 0.3$, $\Delta_1 = 0$, $B_x = 0.3$. (a1) and (b1) show the distribution of probability density profiles of Majorana zero modes, and (a2) and (b2) show the corresponding energy spectra, respectively. Here we have also only shown the part of eigenvalues closest to zero energy. The middle two dots in red in (a2) and (b2) indicate the existence of two Majorana zero modes. The shade of red color on the lattice sites in (a1) and (b1) reflect that the wave functions of Majorana zero modes are strongly localized around the sublattice domain walls.

In Fig.S5, the evolution of boundary energy gap with respect to Zeeman field is shown. One can readily see that the boundary energy gap gets closed and reopened with the increase of B_x , in agreement with the behavior predicted by the low-energy boundary Hamiltonian. In Fig.S6, the numerical results show that each sublattice domain wall hosts one Majorana zero mode when the topological criterion $\min\{B_{b,c}, B_{z,c}\} < B_x < \max\{B_{b,c}, B_{z,c}\}$ is fulfilled. The results indicate that Majorana zero modes at sublattice domain walls can also be achieved in time-reversal symmetry breaking systems. Here it is worth noting that if sublattice-dependent magnetism can be induced on the boundary, Majorana zero modes can be realized at the sublattice domain walls even considering a pure on-site s-wave pairing.

V. TUNING THE POSITIONS OF MAJORANA ZERO MODES BY ELECTRICALLY CONTROLLING THE LOCAL BOUNDARY POTENTIAL

In the main text as well as in Figs.S2 and S6, we have shown that the positions of Majorana zero modes directly follow the change of the positions of sublattice domain walls, indicating that if the terminating sublattices can freely be added or removed, the positions of Majorana zero modes can be manipulated in a site-by-site way. Apparently, this can benefit the detection as well as the implementation of braiding Majorana zero modes. In this section, we show that the positions of Majorana zero modes can also be tuned by electrically controlling the local potential on the boundary, even though the sublattice domain walls are fixed.

To show the tunability, we add a coordinate-dependent on-site potential of the form $\sum_i V_i c_i^\dagger c_i$ to the Hamiltonian, and V_i is chosen to be a nonzero constant only at the neighborhood of the sublattice domain walls. The considered lattice geometry is shown explicitly in Fig.S7. For the convenience of discussion, let us label the lattice sites on the uppermost beard edge from left to right as 1, 2, ..., 12. In Figs.S7(a1) and (a2), the on-site potential is only added to site 1. From the shade of red color on the lattice sites, it is readily found that the site having the highest weight of the probability density of Majorana zero modes becomes site 2. In Figs.S7(b1) and (b2), the on-site potential is added to sites from 1 to 3. Also from the shade of red color on the lattice sites, it is readily found that the site having the highest weight is now shifted from site 2 to site 4. In Figs.S7(c1) and (c2), the on-site potential is added to sites from 1 to 5. It is readily found that the site having the highest weight changes to site 6. The results demonstrate explicitly that the positions of Majorana zero modes can be manipulated site-by-site by controlling the local boundary potential.

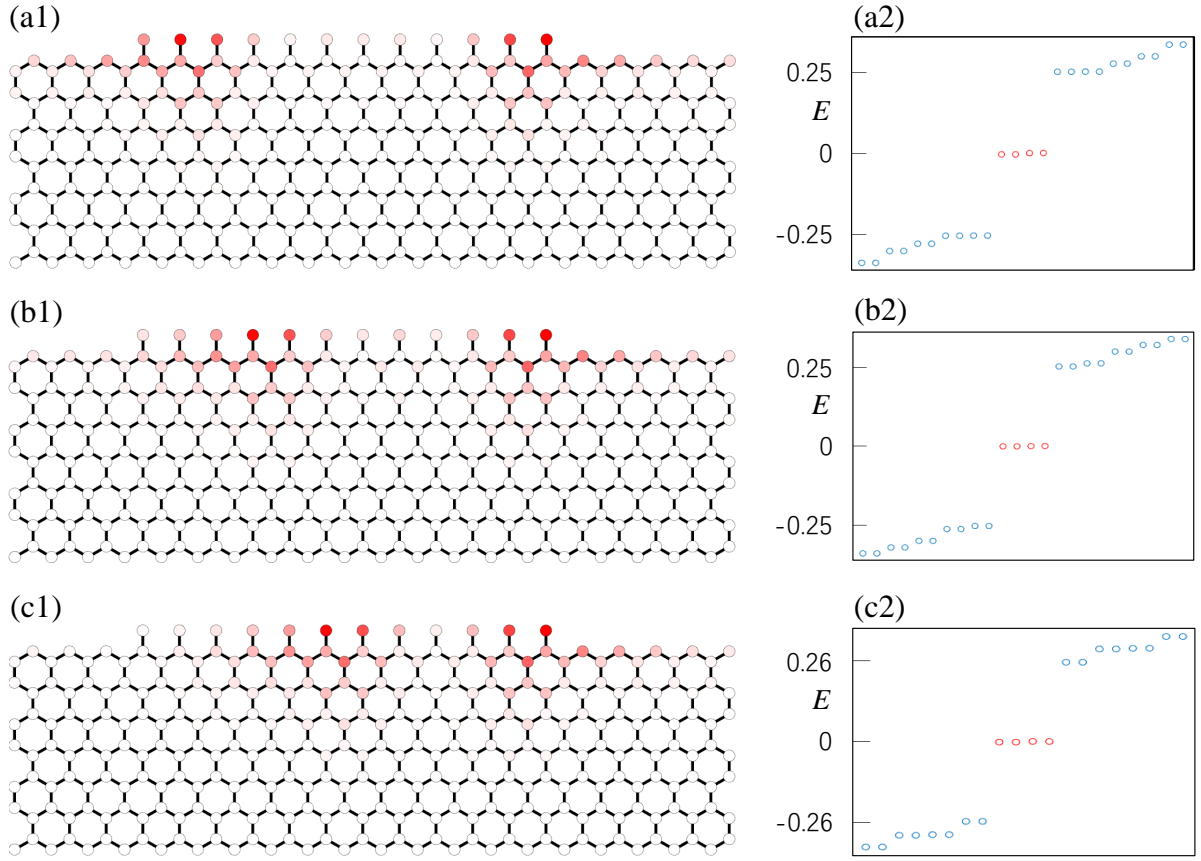


FIG. S7. (Color online) Manipulating the positions of Majorana zero modes by electrically controlling the local potential on the uppermost beard edge. The considered lattice geometry and size are shown explicitly. Here the extended s-wave pairing is considered. In (a1)-(c2), $t = 1$, $\lambda_{so} = 0.1$, $\mu = 0$, $\Delta_0 = \Delta_2 = 0.3$, $\Delta_1 = 0$, $V = 2$. (a1)-(c1) show the distribution of probability density profiles of Majorana zero modes, with the shade of red color reflecting the weight. (a2)-(c2) are the corresponding energy spectra, also only the part of eigenvalues closest to zero energy are shown. On the uppermost beard edge, the lattice sites from left to right are labeled as 1, 2, ..., 12. In (a1) and (a2), the on-site potential V is only added to the lattice site 1. In (b1) and (b2), the on-site potential V is added to lattice sites from 1 to 3. In (c1) and (c2), the on-site potential V is added to lattice sites from 1 to 5. A comparison of the distributions of wave functions of Majorana zero modes in (a1), (b1) and (c1) clearly shows that the positions of Majorana zero modes can be manipulated by controlling the local boundary potential.